universe

MDPI

Article

On the Viscous Ringed Disk Evolution in the Kerr Black Hole Spacetime

Daniela Pugliese [1,*], Zdenek Stuchlík [1] and Vladimir Karas [2]

[1] Research Centre for Theoretical Physics and Astrophysics, Institute of Physics, Silesian University in Opava, Bezručovo Náměstí 13, CZ-74601 Opava, Czech Republic
[2] Astronomical Institute, Czech Academy of Sciences, Boční II 1401, CZ-14100 Prague, Czech Republic
* Correspondence: daniela.pugliese@physics.slu.cz

Abstract: Supermassive black holes **(SMBHs)** are observed in active galactic nuclei interacting with their environments, where chaotical, discontinuous accretion episodes may leave matter remnants orbiting the central attractor in the form of sequences of orbiting toroidal structures, with strongly different features as different rotation orientations with respect to the central Kerr **BH**. Such ringed structures can be characterized by peculiar internal dynamics, where co-rotating and counter-rotating accretion stages can be mixed and distinguished by tori interaction, drying–feeding processes, screening effects, and inter-disk jet emission. A ringed accretion disk (**RAD**) is a full general relativistic model of a cluster of toroidal disks, an aggregate of axi-symmetric co-rotating and counter-rotating disks orbiting in the equatorial plane of a single central Kerr **SMBH**. In this work, we discuss the time evolution of a ringed disk. Our analysis is a detailed numerical study of the evolving **RAD** properties formed by relativistic thin disks, using a thin disk model and solving a diffusion-like evolution equation for an **RAD** in the Kerr spacetime, adopting an initial wavy (ringed) density profile. The **RAD** reaches a single-disk phase, building accretion to the inner edge regulated by the inner edge boundary conditions. The mass flux, the radial drift, and the disk mass of the ringed disk are evaluated and compared to each of its disk components. During early inter-disk interaction, the ring components spread, destroying the internal ringed structure and quickly forming a single disk with timescales governed by ring viscosity prescriptions. Different viscosities and boundary conditions have been tested. We propose that a system of viscously spreading accretion rings can originate as a product of tidal disruption of a multiple stellar system that comes too close to an **SMBH**.

Keywords: black holes;accretion disks; accretion; hydrodynamics; galaxies; actives

Citation: Pugliese, D.; Stuchlík, Z.; Karas, V. On the Viscous Ringed Disk Evolution in the Kerr Black Hole Spacetime. *Universe* **2024**, *10*, 435. https://doi.org/10.3390/universe10120435

Received: 18 October 2024
Revised: 15 November 2024
Accepted: 19 November 2024
Published: 22 November 2024

1. Introduction

In this analysis, we consider a cluster of general relativistic viscous disks orbiting a central Kerr black hole (**BH**). We study the (diffusive) evolution of the disks agglomerate following the approach developed in [1] for a single general relativistic thin disk orbiting a Kerr **BH**, applied here to a general relativistic disk characterized by an internal ringed structure composed of different co-rotating and counter-rotating ring-like components (with respect to the central spinning **BH**).

From the point of view of numerical integration, we address the issue of the condition at the inner edge, focusing on the issue of a single (geometrically thin) disk. We examine ring aggregates with the same relative rotation orientation (*ℓco-rotating*), composed of co-rotating or counter-rotating rings with respect to the central **BH**, and clusters of rings with opposite relative rotation orientation (*ℓcounter-rotating*), constituted by an inner co-rotating ring and an outer counter-rotating ring, or vice versa, by an inner counter-rotating ring and an outer co-rotating ring with respect to the central **BH**. Combined sets of clusters are then considered. We will evaluate the evolution of the fluid density radial drift, the disk mass M_D, and the mass flux as dependent on the **BH** spin, the tori rotation orientation,

and the initial density profiles and spreading. We proceed by adopting an adapted initial condition on the ring's initial density inhomogeneity and spreading, and we investigate the solutions of the diffusion equations for *one* system with an initial wavy (ringed) density profile, modeling the two ℓco-rotating rings with the same viscosity prescription. In order to do this, we shall make use of the ringed accretion disk (**RAD**) model for aggregates of toroidal axis-symmetric disks of co-rotating and counter-rotating fluid structures (tori) orbiting one center supermassive Kerr **BH**, with a symmetry plane coinciding with the equatorial plane of the central Kerr **BH** [2]. The advantage is in the fact that the model strongly binds the disks characteristic to the **BH** defining parameters. The **RAD** frame constrains the initial density profile for aggregates of co-rotating and counter-rotating rings. We use different viscosity prescriptions for tori with different rotation orientations with respect to the central attractor. Doublet, triplet, and quadruplet rings with different relative rotations are also explored.

Aggregates of orbiting toroids can form with strongly different features as different rotation orientations with respect to the central Kerr **BH**, for example, in active galactive nuclei, where disks, forming by several matter remnants around a single central attractor, may contain traces of chaotical accretion episodes.

We should note that the accretion rate can be modified by the interaction between disks, combined with the multi-phase accretion processes of the different components of the cluster. This fact could constitute a mechanism to increase the mass accretion rates and the mass of the supermassive **BHs**. Multi tori orbiting a single attractor can host screening tori. This could be the case, for example, in the double system constituted by an internal co-rotating ring, accompanied by an external counter-rotating toroid that is accreting into the central **BH**. Therefore, this effect would frame multiple and simultaneous accretion phases, including inter-disk accretion and jet shell emission. Observational evidence of these phenomena might be found in a radially stratified emission of the X-ray spectrum.

As the members of a multiple stellar system become tidally disrupted, accretion rings can be produced. We envisage a system of such viscously spreading rings as a model to describe the subsequent evolution and interaction of the debris. In this context, it is interesting to note that, very recently, Peissker et al. (2024) reported on the discovery of a binary system within the S-cluster close to the supermassive **BH** (**SMBH** of mass about $4 \times 10^6 M_\odot$). In fact, the central parsec of the Milky Way's **SMBH** (Sagittarius A*) contains a very dense population of stars: the nuclear star cluster, one of the densest and most massive stellar systems studied so far. Thanks to its relative proximity at a distance of about 8 kpc from us, detailed kinematics of individual stars can be achieved, although the measurements are hampered by obscuration effects along the line of sight and confusion among fast-moving stars. Similar systems can be expected in the nuclei of other quiescent galaxies. Let us emphasize that the galactic center is an extreme example of an inactive nucleus (the accretion rate is very low, no accretion disk is present, and the accretion activity is suppressed); in this case, the signal tidal disruption of stars is expected to be very clean [3].

We first address the case of ℓco-rotating tori, the composition of two independent evolutions, and ℓcounter-rotating rings with different viscosity profiles. The impact on the cluster evolution of the initial density profiles, including the initial ringed components' differences in density and spreading, is evaluated. We expect that within this approximation, due to the combination of ℓcounter-rotating seeds, the evolution observed could be qualitatively similar to ℓco-rotating seed evolution.

The evolution of a geometrically thin disk subjected to a viscous torque was examined in [4,5] with a diffusion-like equation (see also [6,7]). The spreading of a viscous disk in the relativistic regime was also developed by [8–13] (see also [14–16]). Relativistic equations (one-dimensional relativistic equations) reduce to the Keplerian equations in the Newtonian limit. In [17], the cluster diffusive evolution was analyzed following [8–13], describing the evolution of the azimuthal averaged and height integrated disk surface density governed by different viscosity prescriptions and different inner boundary conditions. The case of

BH attractors with spin $a = \pm 0.2$ and with spin $a = \pm 0.9$ were investigated and compared with the limiting case of Schwarzschild static attractors. In this context, the disk's total luminosity, flux, and mass rate were also examined, and it was proved that the disk's luminosity curves present a fingerprint of the initial inner ringed structure of the disk and at different times.

The layout of this paper is as follows. The spacetime metric and constants of motion are introduced in Section 2. Some notes on the ringed accretion disks are presented in Section 2.1.

The evolution of viscous tori is studied in Section 3 following [1], where the dynamics of a viscous gas ring (single thin-disk approximation) orbiting a central Kerr **BH** is discussed. The surface density equation is solved using a perturbation approach adapted to the thin-disk approximation with a low-viscosity assumption. As in [4,5], the general relativistic equation for surface density dynamics is found from the conservation of the energy-momentum tensor for a viscose fluid, including a radiative energy flux and its projection along the flow velocity U^a. Different values of constant viscosity are assumed. **RADs** orbiting a central attractor with spin $a = \pm 0.9$ are explored in Section 3.1. In Section 3.2, **RADs** orbiting a slower spinning **BH** with spin $a = \pm 0.2$ are investigated. The mass flux, the total mass of the disk, and the radial drift of maximum densities in the **RAD** are also studied.

Concluding remarks follow in Section 4. In Appendix A, there are some notes on the conditions of the null flux $\mathcal{F}$ in the frame explored in Section 3.

2. The Spacetime Metric and Constants of Motion

In the Boyer–Lindquist (BL) coordinates $\{t, r, \theta, \phi\}$[1], the Kerr spacetime metric reads

$$ds^2 = -\left(1 - \frac{2Mr}{\Sigma}\right)dt^2 + \frac{\Sigma}{\Delta}dr^2 + \Sigma d\theta^2 + \left[(r^2 + a^2) + \frac{2Mra^2}{\Sigma}\sin^2\theta\right]\sin^2\theta d\phi^2 \quad (1)$$
$$-\frac{4rMa}{\Sigma}\sin^2\theta dt d\phi,$$
$$\Delta \equiv a^2 + r^2 - 2rM \quad \text{and} \quad \Sigma \equiv a^2(1 - \sin^2\theta) + r^2. \quad (2)$$

The equatorial plane, $\sigma \equiv \sin^2\theta = 1$, is a metric symmetry plane coincident with the disk's symmetry plane. Parameter $a = J/M \geq 0$ is the metric spin, where the total angular momentum is J and the gravitational mass parameter is M. A Kerr **BH** is defined by the condition $a \in [0, M]$ with killing horizons $r_- \leq r_+$, where $r_\pm \equiv M \pm \sqrt{M^2 - a^2}$. An extreme Kerr **BH** has dimensionless spin $a/M = 1$, and the non-rotating case $a = 0$ is the Schwarzschild **BH** solution. The spacetime outer ergoregion is $]r_+, r_\epsilon^+]$, where the outer and inner stationary limits $r_\epsilon^\pm$ (ergosurfaces) are given by $r_\epsilon^\pm \equiv M \pm \sqrt{M^2 - a^2(1-\sigma)}$, respectively, where $r_\epsilon^- = 0$ and $r_\epsilon^+ = 2M$ in the equatorial plane $\theta = \pi/2$ ($\sigma = 1$), and $r^+ < r_\epsilon^+$ on $\theta \neq 0$.

(In the following, we will use geometrical units where appropriate to make the reading of dimensionless variables easy, where $r \to r/M$ and $a \to a/M$).

We introduce the constants of motion $(\mathcal{E}, \mathcal{L})$ related to the killing field $\xi_t = \partial_t$ and $\xi_\phi = \partial_\phi$, respectively, with

$$\mathcal{E} = -(g_{t\phi}\dot{\phi} + g_{tt}\dot{t}), \quad \mathcal{L} = g_{\phi\phi}\dot{\phi} + g_{t\phi}\dot{t}, \quad g_{ab}U^aU^b = \kappa\mu^2. \quad (3)$$

$U^a \equiv \{\dot{t}, \dot{r}, \dot{\theta}, \dot{\phi}\}$. The notation $\dot{q}$ is for the derivative of q with respect to the proper time for $\mu > 0$, and $\kappa = -1$ is a normalization constant.

The velocity components (U^t, U^ϕ) are

$$U^t = \frac{g_{\phi\phi}\mathcal{E} + g_{t\phi}\mathcal{L}}{g_{t\phi}^2 - g_{\phi\phi}g_{tt}}, \quad U^\phi = -\frac{g_{t\phi}\mathcal{E} + g_{tt}\mathcal{L}}{g_{t\phi}^2 - g_{\phi\phi}g_{tt}}, \quad (4)$$

where these components also describe the circular orbits in **BL** coordinates. We also introduce the specific angular momentum ℓ and the relativistic angular velocity $\Omega \equiv U^\phi / U^t$, where

$$\ell \equiv \frac{\mathcal{L}}{\mathcal{E}} = -\frac{g_{\phi\phi}U^\phi + g_{\phi t}U^t}{g_{tt}U^t + g_{\phi t}U^\phi} = -\frac{g_{t\phi} + g_{\phi\phi}\Omega}{g_{tt} + g_{t\phi}\Omega}. \tag{5}$$

2.1. Ringed Accretion Disks

Ringed accretion disks (**RADs**) model a cluster of general relativistic toroidal disks orbiting a central Kerr **BH**. In this analysis, we consider the disks sharing the equatorial plane of the Kerr central attractor and the **RAD** being composed by a mixing of co-rotating and counter-rotating rings. Many properties of the aggregate are constrained by the geometry of the Kerr spacetime and, in particular, by the equatorial geodesic structure. This is constituted by the marginally stable circular orbit, $r^{\pm}_{mso}$, the marginally bounded orbit, $r^{\pm}_{mbo}$, and the marginally circular orbit (photon circular orbit), $r^{\pm}_{\gamma}$. Here and in the following, we use the notation $(\pm)$ for counter-rotating and co-rotating motion, respectively.

A free-falling condition for the accretion from the disk inner edge $r_{inner} \in [r^{\pm}_{mbo}, r^{\pm}_{mso}]$ is assumed in many approximations. The assumption that matter in accretion follows, for $r < r_{inner}$, a geodesic motion, having a non-null radial velocity component $U^r \neq 0$, grounds the single ring perturbation for the diffusive equation, and here, we extend this approach to the **RAD** analysis.

Constraints from **RAD** Systems

Here, we summarize the main features of the ringed accretion disk (**RAD**) systems, setting the constraints for the analysis of the diffusive equations of ring clusters orbiting in Kerr spacetimes.

The ringed accretion disks were studied in [2]. **RAD** emerges as a single, geometrically thin accretion disk characterized by an internal ringed structure [2].

To simplify our discussion, below we describe each toroid of the ringed disk as a geometrically thick torus governed by the Polish donut (P-D) model. Nevertheless, **RAD** construction is independent of the adopted model for the ring constituent.

Polish donut (P-D)

In geometrically thick Polish donut (P-D) tori models, the Euler equation describes the axially symmetric stationary general relativity hydrodynamic (GRHD) perfect fluid barotropic tori, governing the force balance in the disk between centrifugal, pressure, and gravitational forces[2].

These are geometrically thick, optical opaque, general relativistic barotropic axially symmetric and stationary toroidal configurations, cooled by advection and composed by a one particle-specie perfect fluid, where $\partial_t \mathrm{Q} = 0$ and $\partial_\phi \mathrm{Q} = 0$, with Q being a generic spacetime tensor. The continuity equation is identically satisfied as a consequence of the symmetries, and the fluid dynamics are governed by the Euler equation only, assuming a barotropic equation of state and fluid orbital motion with $U^\theta = 0$ and $U^r = 0$.

Toroidal surfaces are closed quiescent (C) (without cusp), proto-jets $\mathrm{O}_\times$, and closed-cusped $(\mathrm{C}_\times)$ solutions (proto-jets are open-cusped solutions associated with geometrically thick disks. They are characterized by matter funnels along the direction of the **BH** rotational axis).

In the first and simplest model, a constant fluid-specific angular momentum is assumed ℓ [2,19]; by setting the $\ell =$ constant as a parameter, the maximum density points in the disk are fixed. More specifically, the pressure gradients (defined by the Euler equations) are regulated by the gradients of an effective potential function for the fluid $V_{eff}(r; \ell, a)$ parameterized with a constant specific angular momentum $\ell \equiv \mathcal{L}/\mathcal{E}$.

The force balance in the disk is regulated by an effective potential function and encoded by the Boyer condition of equilibrium configurations of rotating perfect fluids. According

to Boyer's theory on equipressure surfaces applied to a P-D torus, toroidal surfaces are equipotential surfaces with effective potential.

The minima of the effective potential are the maxima of pressure in the torus (torus center r_{center}), and the minima of pressure are the surfaces' cusp $r_\times$ for closed-cusped tori and r_j for proto-jets (see [19]).

The location of pressure extremes is constrained by the spacetime (extended) geodesic structure constituted by radii $\{r^\pm_{mso}, r^\pm_\gamma, r^\pm_{mbo}\}$, the marginally stable and marginally circular (photon) orbit, and the marginally bounded orbits for $\ell^\pm$ and radii $\{r^\pm_{[mbo]}, r^\pm_{[\gamma]}\}$ together, as shown in Figure 1 and defined in Table 1.

The specific angular momentum $\ell^\pm(r;a) \equiv \mathcal{L}^\pm/\mathcal{E}^\pm$ distribution on the equatorial plane for fixed spacetime spin a contains the distributions of all the possible tori centers, $r^\pm_{center} > r^\pm_{mso}$, and cusps, $r^\pm_{inner} \in]r^\pm_\gamma, r^\pm_{mso}[$, where $r^\pm_{inner} \in \{r^\pm_j, r^\pm_\times\}$ for counter-rotating and co-rotating tori, respectively, as shown in Table 1.

The P-D models allow an immediate, simplistic, limiting concept of the inner/outer edge of both quiescent and cusped torii, being defined and identified uniquely by the torus equipotential surface (for quiescent torii) or also by the only angular momentum parameter ℓ, which are constant for each torus for cusped surfaces, governed by the geodesic structure.

These features constitute a model with great advantages and render their adoption extremely useful and predictive; therefore, P-D tori are well known and widely used in the literature also as the initial conditions of the more complex evolution of GRMHD (magnetohydrodynamic) accretion structures (see, for example, ref. [20]).

Clusters constraints

An **RAD** seed (**RAD** of the *order* $n = 2$) is a couple of tori. We can concentrate our attention on two tori with parameters (ℓ_i, ℓ_o) for the inner and outer tori, respectively, with respect to the central **BH**. Introducing notation $\lessgtr$, there is $\mathrm{C}_i < \mathrm{C}_o$ for the ring's relative location (relative location of the tori centers). By construction, the initial data on the ring's seeds describe separated tori. Hence, we have

$$r_{inner}(i) < r_{center}(i) < r_{outer}(i) < r_{inner}(o) < r_{center}(o) < r_{outer}(o), \tag{6}$$

where r_{outer} is the ring's outer edge (with the inner edge $r_{\mathrm{IN}} \in]r^\pm_{mbo}, r^\pm_{mso}]$).

In the **RAD** seeds, we need to introduce the concept of ℓ*co-rotating* tori, defined by the condition $\ell_i\ell_o > 0$, and ℓ*counter-rotating* tori, defined by the relation $\ell_i\ell_o < 0$. The two ℓco-rotating tori can both be co-rotating ($\ell a > 0$) or counter-rotating ($\ell a < 0$) with respect to the central attractor.

We can introduce the spins $\{a_1, a_2, a_3\}$, defined by the crossing of radii of the spacetime geodesic structure (shown in Figure 1 and defined in Table 1), as follows: $a_1 \equiv 0.4740M$: $r^+_{[\mathrm{mbo}]}(a_1) = r^-_{[\gamma]}(a_1)$, $a_2 = 0.461854M$: $r^-_{[\mathrm{mbo}]}(a_2) = r^+_{\mathrm{mso}}(a_2)$ and $a_3 \equiv 0.73688M$: $r^-_{[\gamma]}(a_3) = r^+_{\mathrm{mso}}(a_3)$. Spins $\{a_1, a_2, a_3\}$ identify classes of attractors characterized by the different relative locations of the radii of the geodesic structure. Focusing on a seed with cusped tori, the **RAD** of the order $n = 2$ can be classified into four classes. The first class of seeds is constituted by the tori $\mathrm{C}^\pm_\times < \mathrm{C}^\pm$, which are an ℓco-rotating seed of counter-rotating or co-rotating rings with an inner cusped disk. The seed can be observed in general orbiting any Kerr **BH** attractor. This case also includes any seeds orbiting a Schwarzchild **BH**. The second case is the pair $\mathrm{C}^+_\times < \mathrm{C}^\pm$. We can generalize this case to the pair $()^+ < \mathrm{C}^-$, including an inner accreting $(\mathrm{C}_\times)$ or non-accreting (C) torus, indicated here with notation $()$. These pairs can be observed in all spacetimes with $a \in [0, M]$. For $a \gtrapprox a_3$, the outer torus should be very far from the inner torus to prevent collision, i.e., with $r_{center} > r^-_{[\gamma]}$. However, in spacetimes with $a \in [0, a_2[$ only, the quiescent co-rotating torus C^- approaches the cusped phase, i.e., $r_\times \gtrapprox r^-_{\mathrm{mso}}$, in the **RAD** seed. The third class is the pair $\mathrm{C}^-_\times < \mathrm{C}^\pm$, which can orbit in all spacetimes with $a \in [0, M]$. Finally, the fourth case is constituted by ℓcounter-rotating seeds $\mathrm{C}^-_\times < \mathrm{C}^+_\times$, featuring double accreting disks, formed by an inner co-rotating cusped disk and an outer counter-rotating cusped disk. This **RAD** can be

observed in all Kerr geometries. Whereas, the slower the **BH** ($a \lesssim a_1$), the lower the specific angular momentum ℓ^- of the inner co-rotating torus, and the smaller the tori spacings.

It is worth noting that if the accreting torus is *counter-rotating* with respect to the Kerr attractor, i.e., a $C^+_\times$, then there is *no* inner counter-rotating torus, but a couple may be formed as a $C^+_\times < C^\pm$ or as a $()^- < C^+_\times$ one.

Table 1. Co-rotating and counter-rotating tori in Kerr **BH** spacetimes. $\ell^\pm$ is the fluid specific angular momentum for counter-rotating $(+)$ and co-rotating $(-)$ fluids, respectively. We adopt the notation $q_\bullet \equiv q(r_\bullet)$ for any quantity q evaluated on a radius $r_\bullet$. Radii $\{r^\pm_{mso}, r^\pm_\gamma, r^\pm_{mbo}\}$ are marginally stable and marginally circular (photon) orbits and the marginally bounded orbits for $\ell^\pm$ specific angular momentum. Radii $\{r^\pm_{[mbo]}, r^\pm_{[\gamma]}\}$, together with $\{r^\pm_{mso}, r^\pm_{mbo}, r^\pm_\gamma\}$, constitute the Kerr geometry extended geodesic structure. $r_\times$ (r_j) is the torus (proto-jets) cusp ("inner edge" minimum pressure and density points in the P-D model) and r_{center} is the torus center (maximum pressure and density points in the P-D model) (see Figure 1).

$r^\pm_{[mbo]} : \ell^\pm(r^\pm_{mbo}) = \ell^\pm(r^\pm_{[mbo]}) \equiv \ell^\pm_{mbo}, \quad r^\pm_{[\gamma]} : \ell^\pm(r^\pm_\gamma) = \ell^+(r^+_{[\gamma]}) \equiv \ell^+_\gamma$ $r^\pm_\gamma < r^\pm_{mbo} < r^\pm_{mso} < r^\pm_{[mbo]} < r^\pm_{[\gamma]}$
$\ell^\pm \in \mathbf{L^\pm_1} \equiv]\ell^\pm_{mbo}, \ell^\pm_{mso}[$: quiescent and cusped tori. $r_\times \in]r^\pm_{mbo}, r^\pm_{mso}]$, $r_{center} \in]r^\pm_{mso}, r^\pm_{[mbo]}]$;
$\ell^\pm \in \mathbf{L^\pm_2} \equiv [\ell^\pm_\gamma, \ell^\pm_{\mathrm{mbo}}[$: quiescent tori and proto-jets. $r_j \in]r^\pm_\gamma, r^\pm_{mbo}]$, $r_{center} \in]r^\pm_{[mbo]}, r^\pm_{[\gamma]}]$;
$\ell^\pm \in \mathbf{L^\pm_3} : \ell^\pm < \ell^\pm_\gamma$: quiescent tori, $r_{center} > r^\pm_{[\gamma]}$.

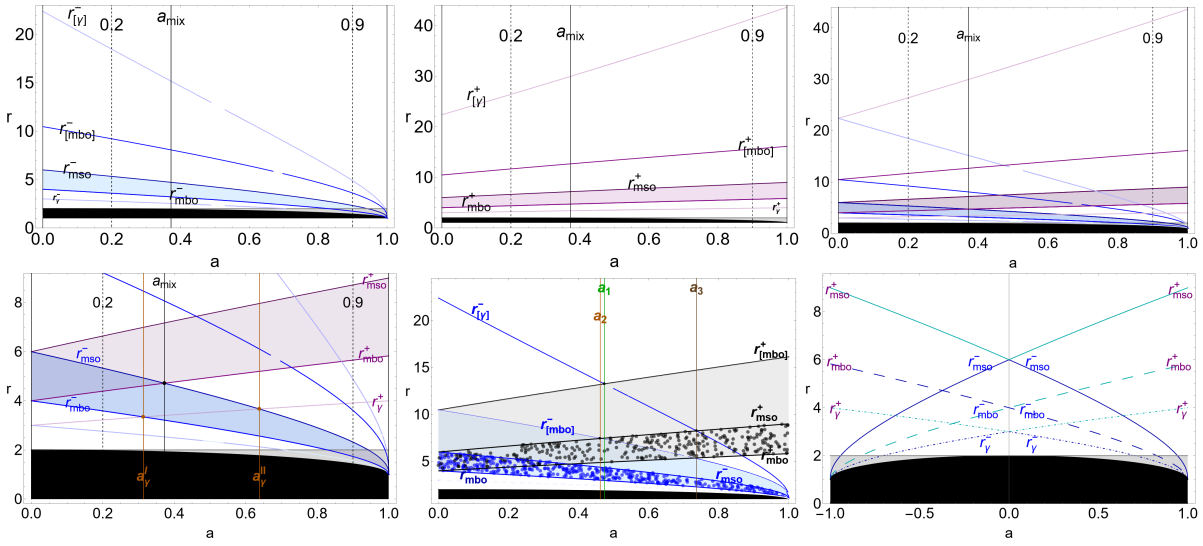

Figure 1. Geodesic structure of the Kerr spacetime. Spin $a_{mix} \equiv 0.37258$, $a^I_\gamma \equiv 0.3137$, $a^{II}_\gamma \equiv 0.6383$, (a_1, a_2) are defined in Section Constraints from **RAD** Systems. The black region is $r < r_+$, with r_+ being the outer horizon of the Kerr geometry, the gray region is $r < r^+_\epsilon$, and $r^+_\epsilon = 2$ is the outer ergosurface on the attractor equatorial plane. Radius $r^\pm_{mso}$ is the marginally stable orbit, $r^\pm_\gamma$ is the marginally circular orbit, and $r^\pm_{mbo}$ is the marginally bounded orbit for counter-rotating and co-rotating particles, respectively. Radii $r^\pm_{[mbo]}, r^\pm_{[\gamma]}$ are in Table 1. **The upper-left** (**center**) panel shows the situation for the co-rotating (counter-rotating) orbits. **The upper-right** panel shows the co-rotating and counter-rotating geodesic structures, and **the left-bottom** panel is a close-up view. Colored stripes in the panels are the regions locating the disk's inner edges $r^\pm_\times \in]r^\pm_{mbo}, r^\pm_{mso}]$. The bottom-center panel shows the co-rotating and counter-rotating geodesic structures where dotted stripes in the panels are the regions locating the disk's inner edges $r^\pm_\times \in]r^\pm_{mbo}, r^\pm_{mso}]$, and colored stripes locate the disk's centers $r^\pm_{center} \in [r^\pm_{[mso]}, r^\pm_{[mbo]}[$. **The bottom-right** panel shows the co-rotating and counter-rotating geodesic structures for **BHs** spins $a \in [-1, 1]$. All quantities are dimensionless.

These configurations are determined by the constraints placed on the inner edge (and in some cases on the torus center and outer edge), which are bounded in the range $]r^{\pm}_{mbo}, r^{\pm}_{mso}]$ (a constraint shared by most accretion disk models).

3. Evolution of Viscous Tori

In [1], the dynamics of a viscous gas ring orbiting a central Kerr **BH** were discussed within the (single) thin-disk approximation. The surface density equation was solved considering the marginally stable orbit as the disk's inner edge, with boundary conditions for the accretion disk model and its time evolution. Following [1], the Kerr background metric is set in Boyer–Lindquist cylindrical coordinates. Using a perturbation approach (the disk height is much smaller than the radial length scale) with a low-viscosity assumption, as in the Keplerian frame, the GR equations for the disk dynamics can be recovered by the conservation of the energy-momentum tensor for a viscose fluid, including a radiative energy flux and its projection along the flow velocity U^a, i.e.,

$$\begin{aligned}&\nabla_a T^{ba} = 0, \quad \nabla_a(\rho U^a) = 0, \quad \text{where} \quad T^{ab} = (\rho + \epsilon + p)U^a U^b + p g^{ab} + S^{ab} + \tau^{ab},\\ &\text{with} \quad \tau^{ab} \equiv U^a q^b + q^a U^b, \quad \text{and} \quad U_a S^{ab} = 0, \quad U_a q^a = 0,\end{aligned} \tag{7}$$

where τ^{ab} can be considered a radiation stress term, ρ is the rest mass density of matter, p the pressure, and ϵ the internal energy. The viscous stress tensor S^{ab} encodes the viscous contribution, and q^a is an energy flux term (radiative energy flow vector)[3]. We also assume

$$S^{ab} = -\nu\rho t^{ab} \quad \text{with} \quad t^{ab} \equiv h^{ac}\nabla_c U^b + h^{bc}\nabla_c U^a - \frac{2}{3}\nabla_c U^c h^{ab}, \tag{8}$$

where the viscosity is $\nu = \nu(r)$, t^{ab} is the trace-free shear tensor, and $h^{ab} \equiv g^{ab} + U^a U^b$ is the projector of the three-dimensional subspace orthogonal onto U^a.

Similarly to **RAD**, it is assumed that $\partial_\phi Q = 0$ for any matter quantity (axially symmetric disk). Moreover, we assume that the rest mass is predominant over the pressure energy density and shear stress. However, in the thin disk approximation, all quantities are independent from z, which is therefore ruled out by vertical integration, and we consider the (vertically integrated) surface density Σ, replacing ρ in the continuity equation[4]. Here, the disks are in circular orbits. We assume the condition $U^r = 0$. Therefore, without viscosity, there would be no radial inflow. Viscosity causes a small perturbation, and we can assume, for the particles gas, a geodesic (Keplerian) motion with velocities $\tilde{U}^a$. These will be deviated by the quantities ξ^a, viscosity terms which are null for $\nu \to 0$. We will only consider terms in first-order in ξ^a (note that $\nu\xi^a$ is a second-term-order perturbation).

Using the approximations in the momentum balance equation, we obtain $\tilde{t}^{ab}$, the shear expression, considering the geodesic four-velocity and the constraint $\tilde{U}_t\tilde{t}^{tr} + \tilde{U}_\phi\tilde{t}^{\phi r} = 0$, where there is

$$\tilde{t}^{\phi r}_{\mp} = \mp\frac{3\sqrt{\frac{M}{r}}\mathcal{T}^{\pm}_{*}\Delta}{2r^3(\mathcal{S}^{\pm}_{*})^{3/2}} \quad \text{where} \quad \mathcal{S}^{\pm}_{*} \equiv r^2 \pm 2a\sqrt{Mr} - 3Mr, \quad \mathcal{T}^{\pm}_{*} \equiv r^2 \pm a\sqrt{Mr} - 2Mr \tag{9}$$

for co-rotating ($\tilde{t}^{\phi r}_{-}$) and counter-rotating ($\tilde{t}^{\phi r}_{+}$) fluids, respectively.

Introducing the following quantities,

$$A_- \equiv \frac{2\sqrt{\frac{r}{M}}\mathcal{S}^{+}_{*}}{r^2 - 3a^2 + 8a\sqrt{Mr} - 6Mr}, \quad B_- \equiv \frac{3\sqrt{Mr}\Delta^2}{2r^2\mathcal{S}^{+}_{*}}, \quad C_- \equiv \frac{\sqrt{\mathcal{S}^{+}_{*}}}{r^2 + a\sqrt{Mr}}, \tag{10}$$

where the mass flux is

$$\mathcal{F}_{\mp} \equiv r\Sigma\xi^r = -A_{\pm}\partial_r(\nu B_{\pm}\Sigma). \tag{11}$$

Here, there is $C_+ = C_-(a \to -a)$, $B_+ = -B_-(a \to -a)$, and $A_+ = -A_-(a \to -a)$, and $\mathcal{F}_-(a) = \mathcal{F}_+(-a) = \mathcal{F}(a)$). Analogously, using the continuity equation, we obtain the equation for the density evolution as follows:

$$\partial_t \Sigma_\pm = C_\pm \partial_r [A_\pm \partial_r (\nu B_\pm \Sigma)] \tag{12}$$

for counter-rotating and co-rotating fluids, respectively[5]. Then, considering Equation (12), $\partial_t \Sigma_- = \partial_t \Sigma_+(a \to -a)$ and $\partial_t \Sigma_-(a = 0) = \partial_t \Sigma_+(a = 0)$. This setup provides the time evolution of a ring under the combined effects of viscous torques and **BH** gravity.

We integrate the evolution equations in Equation (12) by first considering ℓco-rotating rings and then combining the sequence sin ℓcounter-rotating disks sequences. For two **BH** spins, using dimensionless units, we assume a constant viscosity[6] ν. The equations singularities are the orbits $r^\pm_\gamma$ and $r^\pm_{mso}$. Quantity $B_\pm$ is singular on $r^\pm_\gamma$, and quantity $A_\pm$ is singular on $r^\pm_{mso}$ (where $A_\pm$ and $C_\pm$ are null on $r^\pm_\gamma$). However, they are regular on the inner edge in $r_{\rm IN} \in [r^\pm_{mbo}, r^\pm_{mso}[$.

It is worth noting that for a disk (the limiting case of a **RAD** of the order $n = 1$), considering a narrow ring with a Gaussian density distribution, the initial data for the density profile can be set as

$$\Sigma_0(r)|_{n=1} = e^{-\frac{(r-r_0)^2}{b^2}} \quad \text{with} \quad \Sigma(r_{\rm IN})|_{n=1} = 0 \quad \text{and} \quad \mathcal{F}(r_\infty)|_{n=1} = 0, \tag{13}$$

where $r \in [r_{\rm IN}, r_\infty]$ and for $r_{\rm IN} \leq r_{mso}$ ((r_0, b) are constant).

For a **RAD**, the initial density profile ($\Sigma_0 \equiv \Sigma(t = 0, r)$) at $r \geq r_{\rm IN}$ is[7]

$$\Sigma_d(0, r) \equiv \sum_{j=1}^{n} \tilde{c}_j \exp\left[\tilde{d}_j \left(\frac{r - \tilde{r}_j}{\tilde{f}_j}\right)^{\tilde{p}_j}\right], \tag{14}$$

where $\{\tilde{c}_i, \tilde{r}_i, \tilde{d}_i, \tilde{p}_i\}$ are constants to be fixed for each model and can be written as follows:

$$\Sigma_d(0, r)|_{\tilde{p}_j=2, \tilde{d}_j=-1} \equiv \sum_{j=1}^{n} q_j \exp\left[-\left(\frac{r - r_{0_j}}{b_j}\right)^2\right]. \tag{15}$$

Here, $\{r_{0_j}, b_j, q_j\}$ are constants, defining the **RAD** models ($\mathcal{Q}$) listed in Table 2).

Table 2. Initial tori models ($\mathcal{Q}$) for the rings, defined in Equation (15). All the quantities are in dimensionless units. n is the **RAD** order. $r_{\rm IN}$ is the inner ring's inner edge. r_{0_j} is the central radius, b_j is the initial disk spread and fixed r_{0_j}, and parameters q_j and b_j fix the disk mass. ν is the shear viscosity coefficient.

(**A**)	$n = 2$	$\{r_{0_1} = 20, b_1 = 0.1, q_1 = 1/3\}$	$\{r_{0_2} = 26, b_2 = 0.5, q_2 = 1/2\}$	$r_{\rm IN} = 7$
(**B**)	$n = 1$	$\{r_{0_1} = 36, b_1 = 2, q_1 = 1/2\}$	✓	$r_{\rm IN} = 7$
(**C**)	$n = 2, \nu = 2$	$\{r_{0_1} = 10, b_1 = 0.1, q_1 = 1/3\}$	$\{r_{0_2} = 24, b_2 = 1, q_2 = 1/2\}$	$r_{\rm IN} = 2.21$
(**D**)	$n = 2, \nu = 1$	$\{r_{0_1} = 6, b_1 = 0.6, q_1 = 1/3\}$	$\{r_{0_2} = 15, b_2 = 1.1, q_2 = 1/9\}$	$r_{\rm IN} = 2.21$
(**E**)	$n = 2, \nu = 1$	$\{r_{0_1} = 32, b_1 = 0.71, q_1 = 1/3\}$	$\{r_{0_2} = 26, b_2 = 1, q_2 = 1/3\}$	$r_{\rm IN} = 8$
(**F**)	$n = 2, \nu = 1$	$\{r_{0_1} = 6, b_1 = 0.6, q_1 = 1/3\}$	$\{r_{0_2} = 14, b_2 = 1.1, q_2 = 1/9\}$	$r_{\rm IN} = 2.721$
(**G**)	$n = 2, \nu = 2$	$\{r_{0_1} = 10, b_1 = 0.1, q_1 = 1/3\}$	$\{r_{0_2} = 24, b_2 = 1, q_2 = 1/2\}$	$r_{\rm IN} = 2.721$
(**H**)	$n = 2, \nu = 2$	$\{r_{0_1} = 15, b_1 = 1, q_1 = 1/3\}$	$\{r_{0_2} = 34, b_2 = 1, q_2 = 1/2\}$	$r_{\rm IN} = 8$
(**I**)	$n = 2, \nu = 2$	$\{r_{0_1} = 26, b_1 = 0.1, q_1 = 1/3\}$	$\{r_{0_2} = 36, b_2 = 0.5, q_2 = 1/2\}$	$r_{\rm IN} = 6$
(**L**)	$n = 1, \nu = 1$	$\{r_{0_1} = 30, b_1 = 0.1, q_1 = 1/2\}$	✓	$r_{\rm IN} = 6$
(**M**)	$n = 2, \nu = 2$	$\{r_{0_1} = 15, b_1 = 0.1, q_1 = 1/3\}$	$\{r_{0_2} = 24, b_2 = 1, q_2 = 1/2\}$	$r_{\rm IN} = 6$
(**N**)	$n = 2, \nu = 1$	$\{r_{0_1} = 39, b_1 = 0.51, q_1 = 1/3\}$	$\{r_{0_2} = 18, b_2 = 0.1, q_2 = 1/9\}$	$r_{\rm IN} = 6$
(**O**)	$n = 2, \nu = 1$	$\{r_{0_1} = 19, b_1 = 0.1, q_1 = 1/3\}$	$\{r_{0_2} = 36, b_2 = 1, q_2 = 1/3\}$	$r_{\rm IN} = 6$
(**P**)	$n = 2, \nu = 1$	$\{r_{0_1} = 24, b_1 = 0.6, q_1 = 1/3\}$	$\{r_{0_2} = 12, b_2 = 1.1, q_2 = 1/9\}$	$r_{\rm IN} = 6$
(**Q**)	$n = 2, \nu = 2$	$\{r_{0_1} = 18, b_1 = 0.1, q_1 = 1\}$	$\{r_{0_2} = 28, b_2 = 0.1, q_2 = 1/2\}$	$r_{\rm IN} = 6$
(**R**)	$n = 2, \nu = 2$	$\{r_{0_1} = 11, b_1 = 0.1, q_1 = 1/2\}$	$\{r_{0_2} = 34, b_2 = 1, q_2 = 1/2\}$	$r_{\rm IN} = 6$

In order to proceed with the numerical integration, we need to fix the spacetime and fluid parameters that regulate Equation (12). Therefore, in particular, we explored the spin range $a \in [0,1]$ by selecting two representative values of the spin, faster spinning and slower spinning **BHs**, integrating them numerically for all the cases combined, defined according to **(1)** different boundary conditions, **(2)** different initial density profiles, and **(3)** different viscosities. Hence, considering the discussion in Section 2.1, we explore **RAD** evolution in spacetimes with $a = 0.2$ and $a = 0.9$ (see Figure 1 and Table 3). By fixing in this analysis two large and small values of **BH** spin, we evaluate **(i)** the effects of the different rotation orientation of each ring component on the orbiting ringed disk with respect to the central attractor, and **(ii)** the impact of the tori relative rotation in the disk evolution, which is emphasized for faster spinning attractors. By increasing the spin, differences are evident close to and far from the **BH** tori, according to the geodesic structure of the two spins. In this respect, we evaluate the case when the inner torus of a doublet is co-rotating versus counter-rotating (see Figure 1). Tori have different relative rotation orientations and different values of shear viscosity, with initial densities listed in Table 2. Given the problem of symmetries, we can study the co-rotating and counter-rotating rings considering $a = \pm 0.2$ and $a = \pm 0.9$, respectively, investigating ℓco-rotating seeds of co-rotating or counter-rotating rings, set by an initial (modulated) density profile Σ_0 according to Equation (15) for $n = 2$ and within the models $(\mathcal{Q})$ of Table 2. Then, we can investigate the ℓcounter-rotating rings, focusing on the co-evolution of each ℓco-rotating partial solution $(\mathcal{Q}) + (\mathcal{P})$, where $((\mathcal{Q}), (\mathcal{P}))$ are two models of Table 2.

Table 3. Details of the spacetime geodesic structure on the equatorial plane for Kerr **BH** spacetimes with spin $a = 0.2$ and $a = 0.9$, where the outer ergosurface is $r_\epsilon^+ = 2$. Sign $(\pm)$ refers to counter-rotating/co-rotating orbits, respectively. r_{mso} is the marginally stable orbit, r_{mbo} is the marginally circular orbit, and r_γ is the marginally circular orbit, which is also a photon circular orbit. Radii $r_{[\gamma]}$ and $r_{[mbo]}$ constrain the location of tori centers (points of maximum pressure in the disks) and are defined in Table 1. Radius r_+ is the outer **BH** horizon. All quantities are dimensionless.

$a = 0.2$	$r_\gamma^- = 2.76$	$r_{mbo}^- = 3.59$	$r_{mso}^- = 5.33$	$r_{[mbo]}^- = 9.21$	$r_{[\gamma]}^- = 18.48$
$r_+ = 1.98$	$r_\gamma^+ = 3.22$	$r_{mbo}^+ = 4.39$	$r_{mso}^+ = 6.64$	$r_{[mbo]}^+ = 11.67$	$r_{[\gamma]}^+ = 26.41$
$a = 0.9$	$r_\gamma^- = 1.558$	$r_{mbo}^- = 1.732$	$r_{mso}^- = 2.321$	$r_{[mbo]}^- = 3.61$	$r_{[\gamma]}^- = 4.887$
$r_+ = 1.436$	$r_\gamma^+ = 3.91$	$r_{mbo}^+ = 5.657$	$r_{mso}^+ = 8.717$	$r_{[mbo]}^+ = 15.59$	$r_{[\gamma]}^+ = 41.38$

The following five sets of boundary conditions are explored[8]

$$\begin{aligned}
&\textbf{[1]}: \quad \{\Sigma(t, r_{\rm IN}) = 0, \partial_r \Sigma(t, r_{\rm IN}) = 0, \mathcal{F}(t, r_\infty) = 0\}; \quad \textbf{[2]}: \quad \{\partial_r \Sigma(t, r_{\rm IN}) = 0, \mathcal{F}(t, r_\infty) = 0\};\\
&\textbf{[3]}: \quad \{\Sigma(t, r_\infty) = 0, \mathcal{F}(t, r_\infty) = 0\}; \quad \textbf{[4]}: \quad \{\Sigma(t, r_\infty) = 0, \Sigma(t, r_{\rm IN}) = 0, \partial_r \Sigma(t, r_{\rm IN}) = 0\};\\
&\textbf{[5]}: \quad \{\Sigma(t, r_{\rm IN}) = 0, \mathcal{F}(t, r_\infty) = 0\},
\end{aligned} \tag{16}$$

where $\Sigma(0, t) = \Sigma_0$, and the integration has been set in the range[9] $t \in [0, t_f]$ for $r \in [r_{\rm IN}, r_\infty]$. For a single-ring model, we can evaluate the total disk mass as follows[10]

$$\frac{M_D}{2\pi} = \int_{r_{\rm IN}}^{r_\infty} r U^t \Sigma dr, \tag{17}$$

and for n **RAD** components, we considered the contribution of all rings and the sum of each ring mass contribution, dividing into subsets the integration total range $[r_{\rm IN}, r_\infty]$ (see Figure 22). The independent evolution of combined ℓcounter-rotating **RAD** seeds is studied for spin $a = \pm 0.9$ in Section 3.1 and Figures 3, 5, 7, 9 and 11), and for spin $a = \pm 0.2$, Section 3.2 and Figures 13, 15, 17, 19 and 24), focusing on the following composite systems:

–Figures 3, 9 and 11. The ℓco-rotating triplet of counter-rotating rings $(\mathbf{A}+\mathbf{B}):\mathrm{C}_+(\mathbf{A})<\mathrm{C}_+(\mathbf{A})<\mathrm{C}_+(\mathbf{B})$.

The ℓcounter-rotating triplet $(\mathbf{B}+\mathbf{C}):\mathrm{C}_-(\mathbf{C})<\mathrm{C}_-(\mathbf{C})<\mathrm{C}_+(\mathbf{B})$.

The ℓcounter-rotating triplet $(\mathbf{B}+\mathbf{D}):\mathrm{C}_-(\mathbf{D})<\mathrm{C}_-(\mathbf{D})<\mathrm{C}_+(\mathbf{B})$.

The ℓco-rotating quadruplet of co-rotating rings $(\mathbf{D}+\mathbf{C}):\mathrm{C}_-(\mathbf{D})<\mathrm{C}_-(\mathbf{C})<\mathrm{C}_-(\mathbf{D})<\mathrm{C}_-(\mathbf{C})$.

–Figures 5 and 7. The ℓcounter-rotating quadruplet $(\mathbf{E}+\mathbf{F}):\mathrm{C}_-(\mathbf{F})<\mathrm{C}_-(\mathbf{F})<\mathrm{C}_+(\mathbf{E})<\mathrm{C}_+(\mathbf{E})$.

The ℓcounter-rotating quadruplet $(\mathbf{H}+\mathbf{G}):\mathrm{C}_-(\mathbf{G})<\mathrm{C}_+(\mathbf{H})<\mathrm{C}_-(\mathbf{G})<\mathrm{C}_+(\mathbf{H})$.

The ℓco-rotating quadruplet of co-rotating rings $(\mathbf{F}+\mathbf{G}):\mathrm{C}_-(\mathbf{F})<\mathrm{C}_-(\mathbf{G})<\mathrm{C}_-(\mathbf{F})<\mathrm{C}_-(\mathbf{G})$.

–Figures 13, 19, and 24. The ℓco-rotating triplet of counter-rotating rings $(\mathbf{I}+\mathbf{L}):\mathrm{C}_+(\mathbf{I})<\mathrm{C}_+(\mathbf{L})<\mathrm{C}_+(\mathbf{I})$.

The ℓcounter-rotating triplet $(\mathbf{L}+\mathbf{M}):\mathrm{C}_-(\mathbf{M})<\mathrm{C}_-(\mathbf{M})<\mathrm{C}_+(\mathbf{L})$.

The ℓco-rotating quadruplet of co-rotating rings $(\mathbf{M}+\mathbf{N}):\mathrm{C}_-(\mathbf{M})<\mathrm{C}_-(\mathbf{N})<\mathrm{C}_-(\mathbf{M})<\mathrm{C}_-(\mathbf{N})$.

The ℓcounter-rotating triplet $(\mathbf{L}+\mathbf{N}):\mathrm{C}_-(\mathbf{N})<\mathrm{C}_+(\mathbf{L})<\mathrm{C}_-(\mathbf{N})$.

–Figures 15 and 17. The ℓcounter-rotating quadruplet $(\mathbf{O}+\mathbf{P}):\mathrm{C}_-(\mathbf{P})<\mathrm{C}_+(\mathbf{Q})<\mathrm{C}_-(\mathbf{P})<\mathrm{C}_+(\mathbf{Q})$.

The ℓco-rotating quadruplet of co-rotating rings $(\mathbf{Q}+\mathbf{P}):\mathrm{C}_-(\mathbf{P})<\mathrm{C}_-(\mathbf{Q})<\mathrm{C}_-(\mathbf{P})<\mathrm{C}_-(\mathbf{Q})$.

The ℓcounter-rotating quadruplet $(\mathbf{R}+\mathbf{Q}):\mathrm{C}_+(\mathbf{R})<\mathrm{C}_-(\mathbf{Q})<\mathrm{C}_-(\mathbf{Q})<\mathrm{C}_+(\mathbf{R})$.

As is also confirmed in the analysis of [17], the diffusive evolution of a ringed disk can be described in four phases (analogue to a **RAD** evolution in a Keplerian frame). Initially, we observe the rings spreading inside the **RAD**. Consequently, the internal ringed structure changes by leveling the density differences among the disks. This phase is characterized by marked internal activity with interaction among each ringed component. Following this evolution, an internal density maximum appears, signaling the formation of a single disk. The final phase is, therefore, dominated by single-disk structure evolution. The predominant dynamics at the origin are regulated mainly by the **RAD** boundary conditions.

Concentrating on the early stages of **RAD** evolution, we will focus on the description of the phases preceding the disappearance of the internal structure, distinguishing the **RAD** internal dynamics with their inter-disk activity. In this phase, the densities maximum generally spreads towards the origin, and the disk's outer edges move to larger radii. Note, assuming the inner edge is close to the marginally stable orbit, a ring evolution (at small Σ) proceeds similarly to the non-relativistic setup. On the other hand, the low viscosity approximation cannot hold well for the later stages of ring cluster evolution. It is clear that the accreting matter from the inner edge of the outer ring of the cluster can have an unperturbed radial component $\tilde{U}^r \neq 0$[11].

In Section 3.1, we consider **RADs** orbiting a central attractor with spin $a = \pm 0.9$, and in Section 3.2, **RADs** orbiting a slower spinning **BH** with spin $a = \pm 0.2$ are explored.

*3.1. **BH** Attractors with Spin $a = \pm 0.9$*

In this section, we consider **RAD** orbiting **BH** attractors with spin $a = \pm 0.9$ (see Table 3). The ℓco-rotating rings surface density evolution in the **BH** spacetimes with $a = \pm 0.9$ is shown in Figure 2; co-rotating and counter-rotating fluids are also discussed. In this case, the models $\{(\mathbf{A}), (\mathbf{B}), (\mathbf{C}), (\mathbf{D})\}$ of Table 2 are considered (note, model $(\mathbf{B})$ (upper-right panel) is composed of one counter-rotating ring), with the boundary condition $[\mathbf{1}]$ of Equation (16) and different values of the viscosity coefficient ν. With the analysis of the model $(\mathbf{B})$, we can compare single-ring diffusive evolution with **RAD** diffusive

evolution. In condition [**1**], seed evolution is characterized by a building-up of matter close to the origin (inner edge of the inner **RAD** ring) at later stages of evolution (more evident in the counter-rotating case). Focusing on the initial phases of seed evolution featuring **RAD** inner structure evolution with ring interaction, the process timescales of the inner ringed structure re-modulation depend on initial ring spreading and density (the process appears less dependent on different viscosity values). The first phases of spread and merging are fast, rapidly followed by the formation of one maximum density for a newly formed one-ring structure located close to the initial density maximum with a radial drift velocity. The disk in this phase can retain a modulated inner density profile depending on the tori's initial spreading and separation (see model (**D**)). In the analysis of combined seeds in Figure 3, we also consider the combined ℓco-rotating rings quadruplets or triplets compared with the case of the ℓco-rotating solutions of **RAD** diffusive equations.

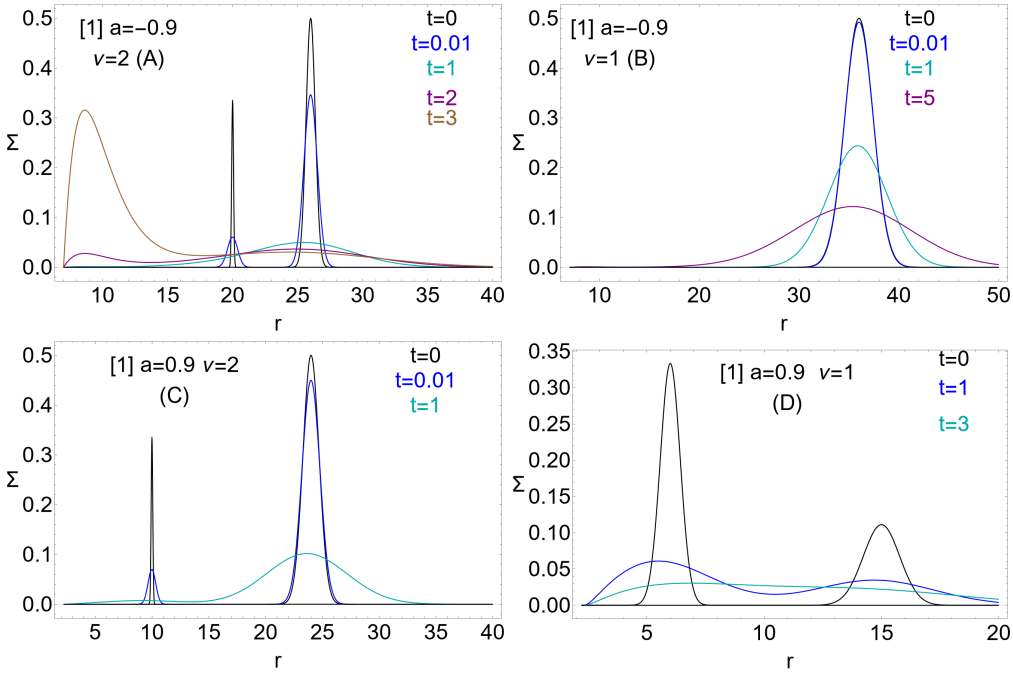

Figure 2. Evolution of the surface density Σ for the ℓco-rotating rings orbiting in the Kerr spacetime with $a = \mp 0.9$ for counter-rotating $(+)$ and co-rotating $(-)$ flows, respectively, at different times t signed on the panel (see Table 3). The initial density profiles are the models $\{(\mathbf{A}), (\mathbf{B}), (\mathbf{C}), (\mathbf{D})\}$ of Table 2, with the boundary condition [**1**] of Equation (16). ν is the viscosity coefficient. Note, model (**B**) (**upper-right** panel) is composed of one counter-rotating ring). All the quantities are dimensionless.

The combination of the ℓcounter-rotating seeds in Figure 3 shows that the evolution is qualitatively similar to the ℓco-rotating seed evolution. In this combined analysis, the radial range of integration is fixed considering the two seeds' different inner edges. Interestingly, there is the permanence of the modulated inner structure at later times, with the inner dynamics not affecting the inner (and outer) **RAD** region's evolution.

The boundary condition [**2**] of Equation (16) has been tested in Figure 4. In the (**F**) model, we note a phase of matter decreasing at the seed's inner edge, which can also be seen in the seed (ℓcounter-rotating) combination in Figure 5.

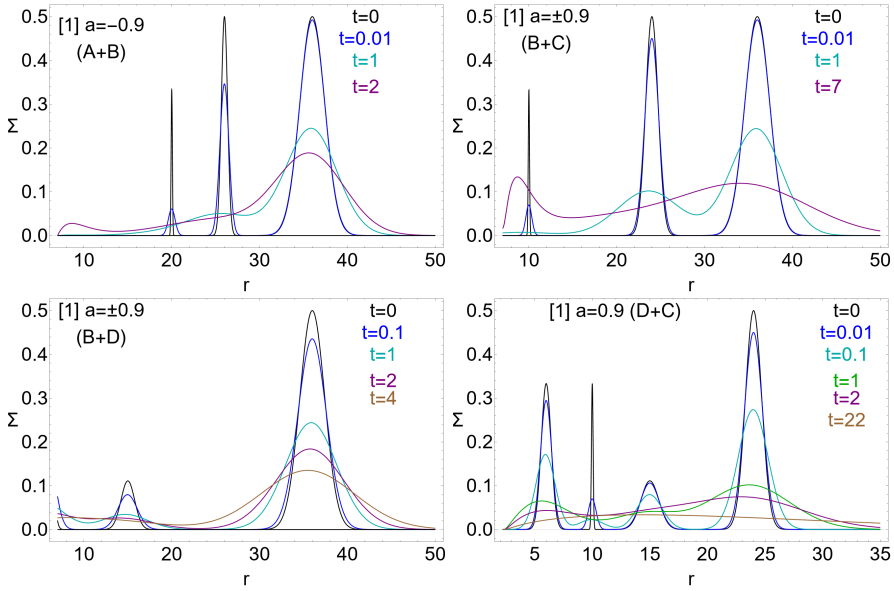

Figure 3. Combined (independent) evolution of the surface densities Σ of ℓcounter-rotating rings couples composed by two sets of ℓco-rotating rings from the integration in Figure 2 for the Kerr spacetime with spin $a = \pm 0.9$ for co-rotating and counter-rotating fluids, respectively (see Table 3). Dimensionless time values for the different stages of evolution are signed on the panel. All the quantities are dimensionless. The initial density profiles are the combinations of models $\{(\mathbf{A}), (\mathbf{B}), (\mathbf{C}), (\mathbf{D})\}$ defined in Table 2, with boundary condition [**1**] of Equation (16). ν is the viscosity coefficient. Note, system $(\mathbf{A} + \mathbf{B})$ is an ℓco-rotating triplet of counter-rotating tori $\mathrm{C}_+(\mathbf{A}) < \mathrm{C}_+(\mathbf{A}) < \mathrm{C}_+(\mathbf{B})$. Notation $(\pm)$ is for counter-rotating/co-rotating fluids, respectively. System $(\mathbf{B} + \mathbf{C})$ is the ℓcounter-rotating triplet $\mathrm{C}_-(\mathbf{C}) < \mathrm{C}_-(\mathbf{C}) < \mathrm{C}_+(\mathbf{B})$. System $(\mathbf{B} + \mathbf{D})$ is the ℓcounter-rotating triplet $\mathrm{C}_-(\mathbf{D}) < \mathrm{C}_-(\mathbf{D}) < \mathrm{C}_+(\mathbf{B})$. System $(\mathbf{D} + \mathbf{C})$ is the ℓco-rotating quadruplet of co-rotating rings: $\mathrm{C}_-(\mathbf{D}) < \mathrm{C}_-(\mathbf{C}) < \mathrm{C}_-(\mathbf{D}) < \mathrm{C}_-(\mathbf{C})$. The radial range has been adapted according to the combination of the independent integrations ranges. The viscosity coefficients ν are fixed according to Figure 2.

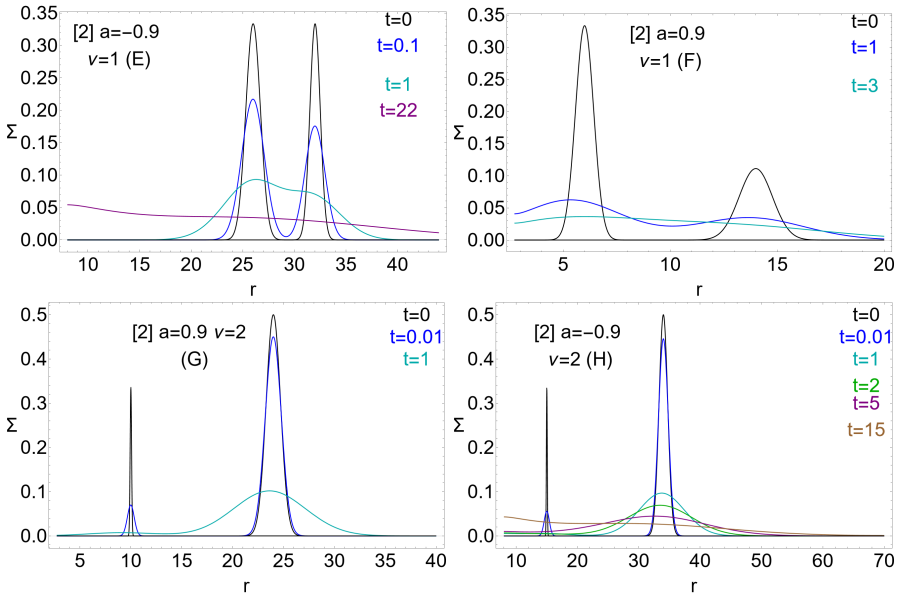

Figure 4. Evolution of the surface density Σ (ℓco-rotating rings) in the Kerr metric with spin $a = \mp 0.9$ at different times t for counter-rotating and co-rotating fluids, respectively (see Table 3). All the quantities are dimensionless. The initial density profiles are the models $\{(\mathbf{E}), (\mathbf{F}), (\mathbf{G}), (\mathbf{H})\}$ of Table 2), with the boundary condition [**2**] of Equation (16). ν is the viscosity coefficient.

In Figure 6, conditions [**3**] of Equation (16) are tested. The building-up phase at the inner edge is evidenced together with the (rapid) destruction of the **RAD** inner structure, also characterizing the ℓcounter-rotating **RAD** in the combined evolution of Figure 7. The persistence of a modulated inner-density structure at the stage of one single disk could be seen as fingerprint of a **RAD** initial stage, constituted by ring aggregates characterized by different viscosity prescriptions.

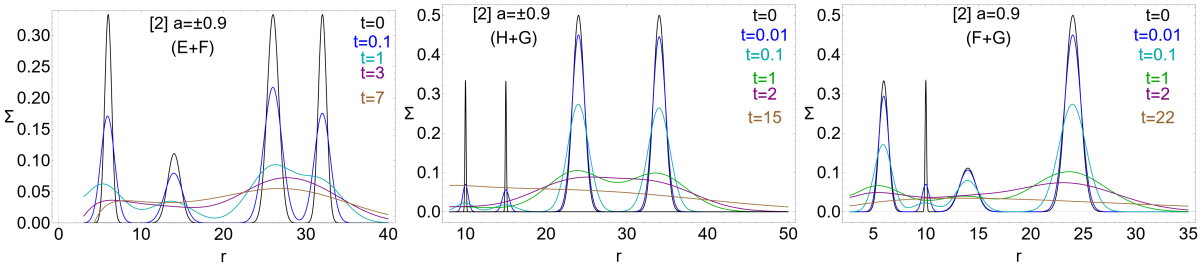

Figure 5. Combined (independent) evolution of the surface densities Σ of the ℓcounter-rotating rings couples composed by two clusters of ℓco-rotating disks from the integration in Figure 4. The initial density profiles are the combinations of models $\{(\mathbf{E}),(\mathbf{F}),(\mathbf{G}),(\mathbf{H})\}$ defined in Table 2), with boundary condition [**2**] of Equation (16). ν is the viscosity coefficient. System $(\mathbf{E}+\mathbf{F})$ is the ℓcounter-rotating quadruplet $C_-(\mathbf{F}) < C_-(\mathbf{F}) < C_+(\mathbf{E}) < C_+(\mathbf{E})$. System $(\mathbf{H}+\mathbf{G})$ is the ℓcounter-rotating quadruplet $C_-(\mathbf{G}) < C_+(\mathbf{H}) < C_-(\mathbf{G}) < C_+(\mathbf{H})$. System $(\mathbf{F}+\mathbf{G})$ is the ℓco-rotating quadruplet of co-rotating rings $C_-(\mathbf{F}) < C_-(\mathbf{G}) < C_-(\mathbf{F}) < C_-(\mathbf{G})$. The radial range has been adapted according to the combination of the independent integrations ranges. The viscosity coefficients ν are fixed according to Figure 4.

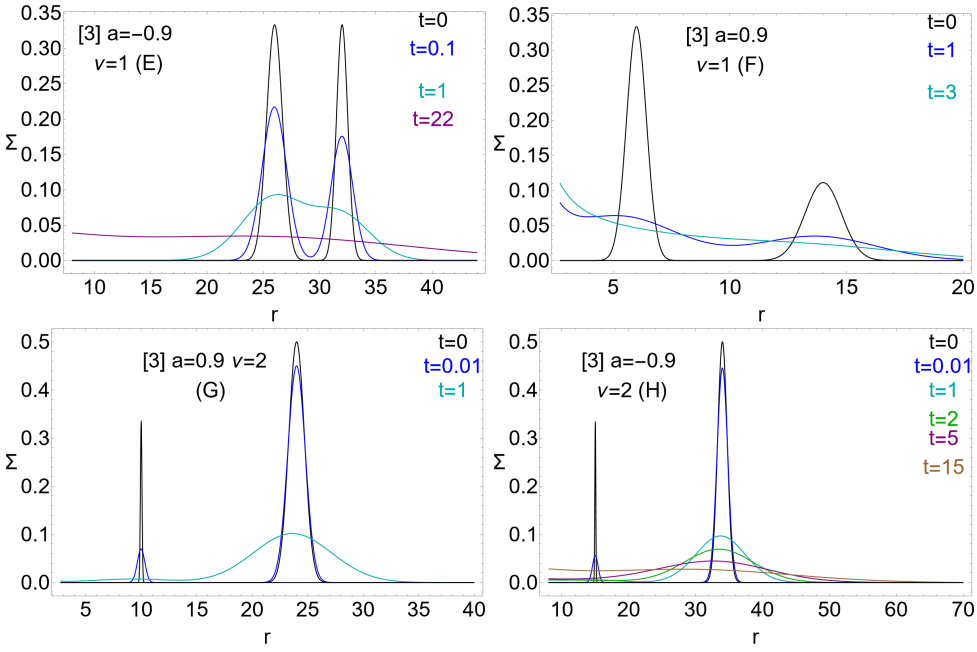

Figure 6. Evolution of the surface density Σ (ℓco-rotating rings) in the Kerr metric with spin $a = \pm 0.9$ for co-rotating and counter-rotating fluids, respectively, at different times t signed on the panels (see Table 3). All the quantities are dimensionless. The initial density profiles are the models $\{(\mathbf{E}),(\mathbf{F}),(\mathbf{G}),(\mathbf{H})\}$ of Table 2), with the boundary condition [**3**] of Equation (16). ν is the viscosity coefficient.

Boundary conditions [**4**] and [**5**] of Equation (16) are tested in Figure 8 and Figure 9, respectively, for the initial density profiles $\{(\mathbf{A}),(\mathbf{B}),(\mathbf{C}),(\mathbf{D})\}$ of Table 2. Remarkably, the **RAD** seed evolution is then similar to the evolution in Figure 2.

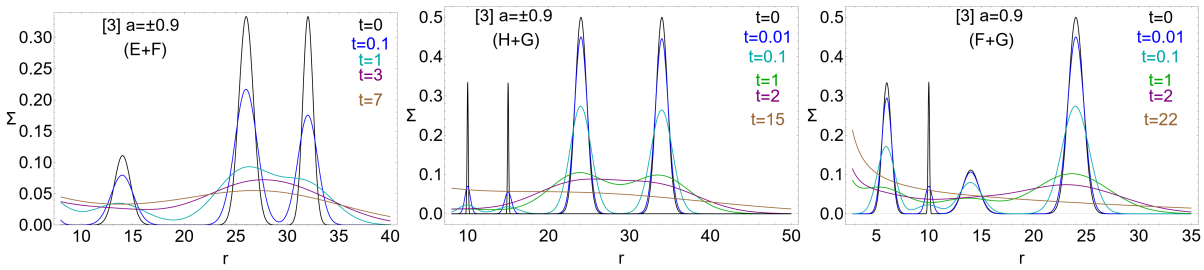

Figure 7. Combined (independent) evolution of the surface densities Σ of the ℓcounter-rotating ring couples composed by two sets of ℓco-rotating rings from the integration in Figure 6. The initial density profiles are the combinations of models $\{(\mathbf{E}), (\mathbf{F}), (\mathbf{G}), (\mathbf{H})\}$ defined in Table 2, with boundary condition [**3**] of Equation (16). ν is the viscosity coefficient. System $(\mathbf{E}+\mathbf{F})$ is the ℓcounter-rotating quadruplet $\mathrm{C}_-(\mathbf{F}) < \mathrm{C}_-(\mathbf{F}) < \mathrm{C}_+(\mathbf{E}) < \mathrm{C}_+(\mathbf{E})$. System $(\mathbf{H}+\mathbf{G})$ is the ℓcounter-rotating quadruplet $\mathrm{C}_-(\mathbf{G}) < \mathrm{C}_+(\mathbf{H}) < \mathrm{C}_-(\mathbf{G}) < \mathrm{C}_+(\mathbf{H})$. System $(\mathbf{F}+\mathbf{G})$ is the ℓco-rotating quadruplet of co-rotating rings $\mathrm{C}_-(\mathbf{F}) < \mathrm{C}_-(\mathbf{G}) < \mathrm{C}_-(\mathbf{F}) < \mathrm{C}_-(\mathbf{G})$. The radial range has been adapted according to the combination of the independent integrations ranges. The viscosity coefficients ν are fixed according to Figure 6.

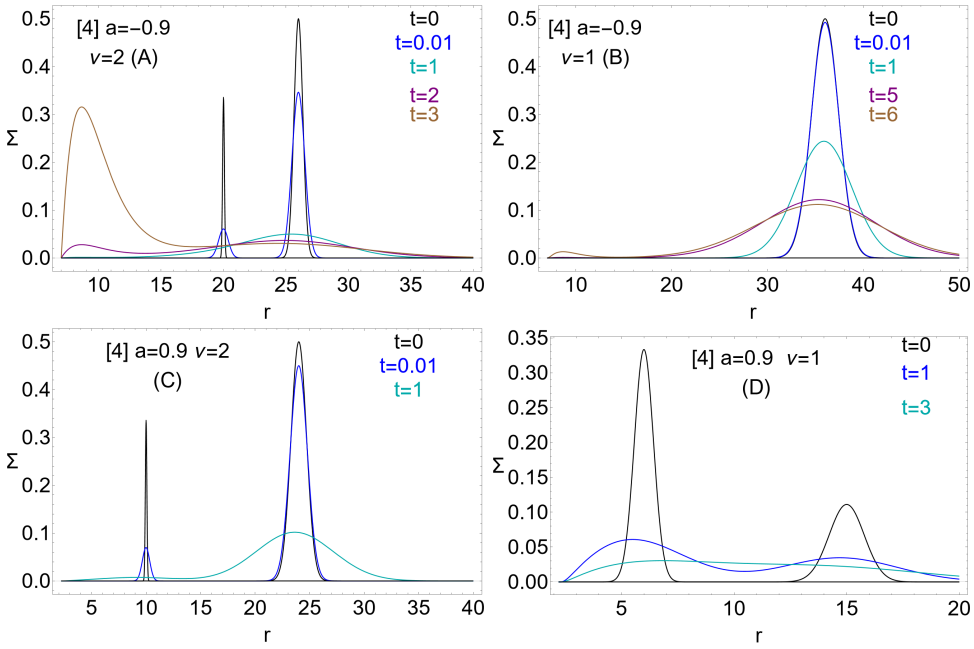

Figure 8. Evolution of the surface density Σ (ℓco-rotating rings) at different times t signed on the panels in the Kerr metric with spin $a = \mp 0.9$ (for counter-rotating and co-rotating fluids, respectively) (see Table 3). The initial density profiles are the models $\{(\mathbf{A}), (\mathbf{B}), (\mathbf{C}), (\mathbf{D})\}$ of Table 2, with the boundary condition [**4**] of Equation (16). ν is the viscosity coefficient. Note, model $(\mathbf{B})$ (**upper-right** panel) is composed of one counter-rotating ring).

Different (inner) boundary conditions on the **RAD** edges affect mostly the **RAD** evolution rather then the inner structure evolution generally resolved in the early times (see, for example, Figures 10 and 11).

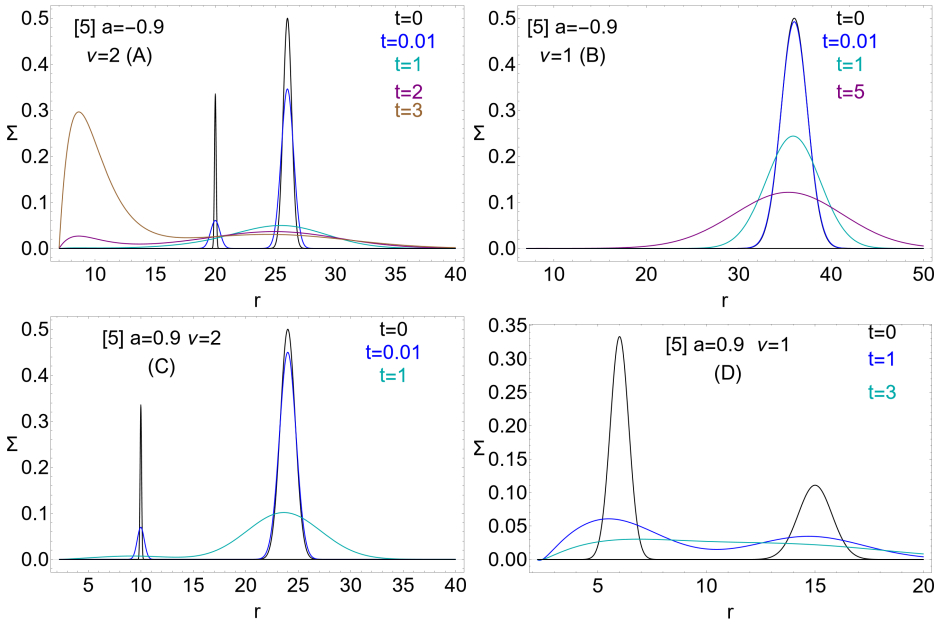

Figure 9. Evolution of the surface density Σ (ℓco-rotating rings) at different times t signed on the panels in the Kerr metric with spin $a = \pm 0.9$ for co-rotating and counter-rotating fluids, respectively (see Table 3). The initial density profiles are the models $\{(\mathbf{A}), (\mathbf{B}), (\mathbf{C}), (\mathbf{D})\}$ of Table 2, with the boundary condition [**5**] of Equation (16). ν is the viscosity coefficient. Note, model $(\mathbf{B})$ (**upper-right** panel) is composed of one counter-rotating ring).

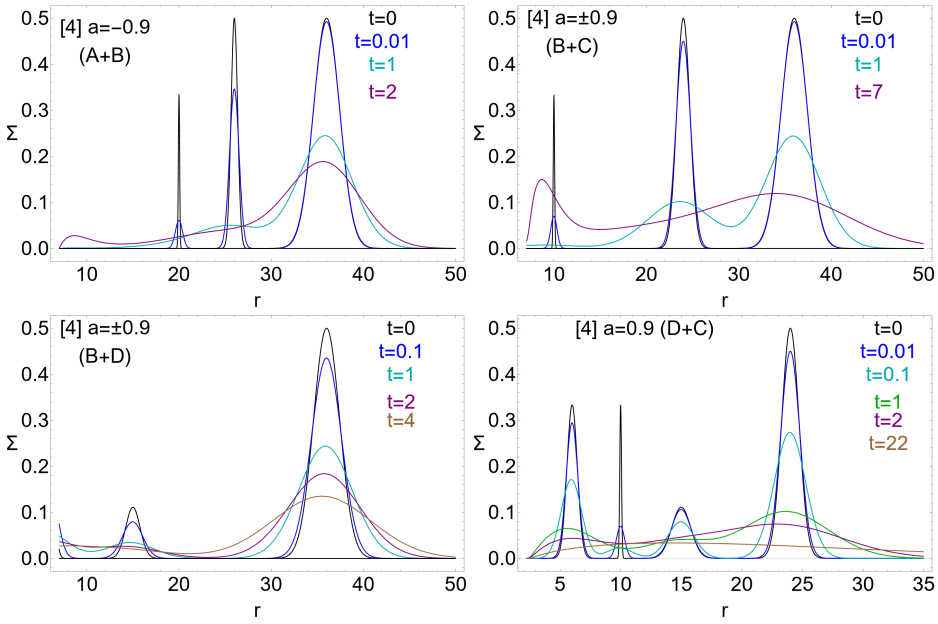

Figure 10. Combined (independent) evolution of the surface densities Σ of the ℓcounter-rotating ring couples composed by two sets of ℓco-rotating rings from the integration in Figure 8. The initial density profiles are combinations of models $\{(\mathbf{A}), (\mathbf{B}), (\mathbf{C}), (\mathbf{D})\}$ defined in Table 2, with boundary condition [**4**] of Equation (16). ν is the viscosity coefficient. Note, system $(\mathbf{A} + \mathbf{B})$ is a ℓco-rotating triplet of counter-rotating tori $\mathrm{C}_+(\mathbf{A}) < \mathrm{C}_+(\mathbf{A}) < \mathrm{C}_+(\mathbf{B})$. Notation $(\pm)$ is for counter-rotating/co-rotating fluids, respectively). System $(\mathbf{B} + \mathbf{C})$ is the ℓcounter-rotating triplet $\mathrm{C}_-(\mathbf{C}) < \mathrm{C}_-(\mathbf{C}) < \mathrm{C}_+(\mathbf{B})$. System $(\mathbf{B} + \mathbf{D})$ is the ℓcounter-rotating triplet $\mathrm{C}_-(\mathbf{D}) < \mathrm{C}_-(\mathbf{D}) < \mathrm{C}_+(\mathbf{B})$. System $(\mathbf{D} + \mathbf{C})$ is the ℓco-rotating quadruplet of co-rotating rings: $\mathrm{C}_-(\mathbf{D}) < \mathrm{C}_-(\mathbf{C}) < \mathrm{C}_-(\mathbf{D}) < \mathrm{C}_-(\mathbf{C})$. The radial range has been adapted according to the combination of the independent integrations ranges. The viscosity coefficients ν are fixed according to Figure 8.

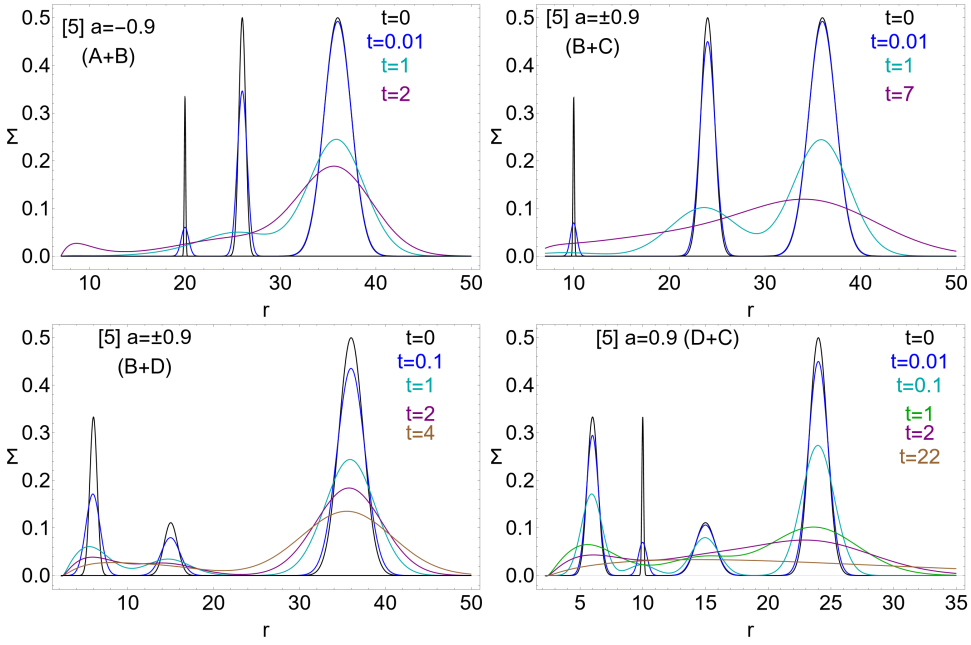

Figure 11. Combined (independent) evolution of the surface densities Σ of the ℓcounter-rotating rings couples composed of two sets of ℓco-rotating rings from the integration in Figure 9. The initial density profiles are the combinations of models $\{(\mathbf{A}), (\mathbf{B}), (\mathbf{C}), (\mathbf{D})\}$ defined in Table 2, with boundary condition $[\mathbf{5}]$ of Equation (16). ν is the viscosity coefficient. Note, system $(\mathbf{A}+\mathbf{B})$ is an ℓco-rotating triplet of counter-rotating tori $\mathrm{C}_+(\mathbf{A}) < \mathrm{C}_+(\mathbf{A}) < \mathrm{C}_+(\mathbf{B})$. Notation $(\pm)$ is for counter-rotating/co-rotating fluids, respectively). System $(\mathbf{B}+\mathbf{C})$ is the ℓcounter-rotating triplet $\mathrm{C}_-(\mathbf{C}) < \mathrm{C}_-(\mathbf{C}) < \mathrm{C}_+(\mathbf{B})$. System $(\mathbf{B}+\mathbf{D})$ is the ℓcounter-rotating triplet $\mathrm{C}_-(\mathbf{D}) < \mathrm{C}_-(\mathbf{D}) < \mathrm{C}_+(\mathbf{B})$. System $(\mathbf{D}+\mathbf{C})$ is the ℓco-rotating quadruplet of co-rotating rings: $\mathrm{C}_-(\mathbf{D}) < \mathrm{C}_-(\mathbf{C}) < \mathrm{C}_-(\mathbf{D}) < \mathrm{C}_-(\mathbf{C})$. The radial range has been adapted according to the combination of the independent integrations ranges. The viscosity coefficients ν are fixed according to Figure 9.

*3.2. **BH** Attractors with Spin $a = \pm 0.2$*

In Figures 12 and 13, we consider clusters orbiting **BHs** with spin $a = \pm 0.2$. Similarly to the case in Figure 2, boundary conditions $[\mathbf{1}]$ of Equation (16) are considered here for the initial density profiles $\{(\mathbf{I}), (\mathbf{L}), (\mathbf{M}), (\mathbf{N})\}$ of Table 2, where model $(\mathbf{L})$ (upper-right panel) is composed of one counter-rotating ring. The destruction of the inner **RAD** structure is followed by the formation of an inner maximum density also present during later stages of **RAD** evolution.

Boundary conditions $[\mathbf{2}]$ are tested in Figures 14 and 15, where, for the $(\mathbf{P})$ model, an increase in mass at the inner edge followed by a decreasing phase during later stages of evolution is noted.

From the analysis of the boundary condition $[\mathbf{3}]$ applied to the $\{(\mathbf{O}), (\mathbf{P}), (\mathbf{Q}), (\mathbf{R})\}$ models of Figure 16, we see that, after the leveling of the inner ringed structure, the single maximum density of the final disk appears to be affected mostly by the spreading of the initial ring cluster.

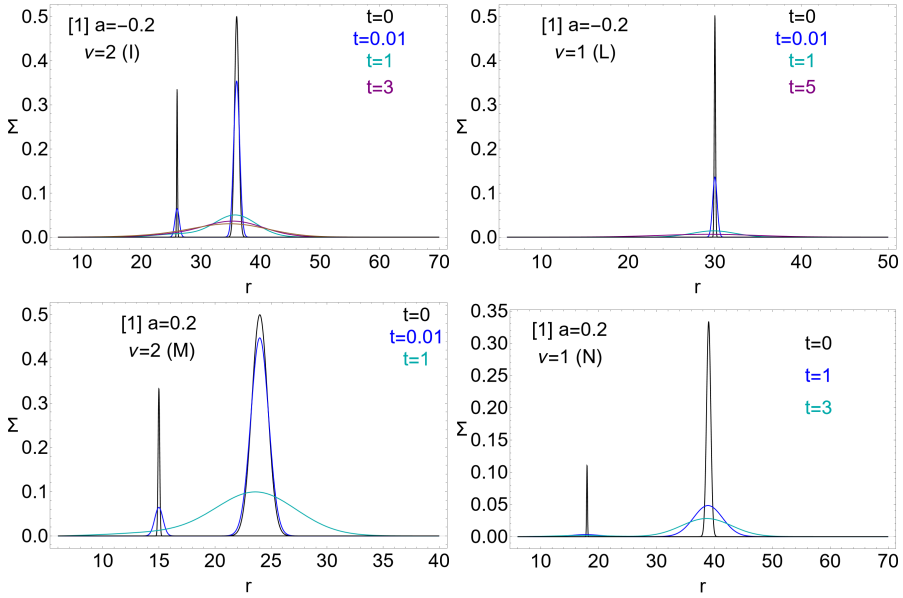

Figure 12. Evolution of the surface density Σ (ℓco-rotating rings) in the Kerr metric with spin $a = \pm 0.2$ for co-rotating and counter-rotating fluids, respectively (see Table 3). All the quantities are dimensionless. Dimensionless time values for the different stages of evolution are signed on the panel. The initial density profiles are the models $\{(\mathbf{I}), (\mathbf{L}), (\mathbf{M}), (\mathbf{N})\}$ of Table 2, with the boundary condition $[\mathbf{1}]$ of Equation (16). ν is the viscosity coefficient. Note, model $(\mathbf{L})$ (**upper-right** panel) is composed of one counter-rotating ring).

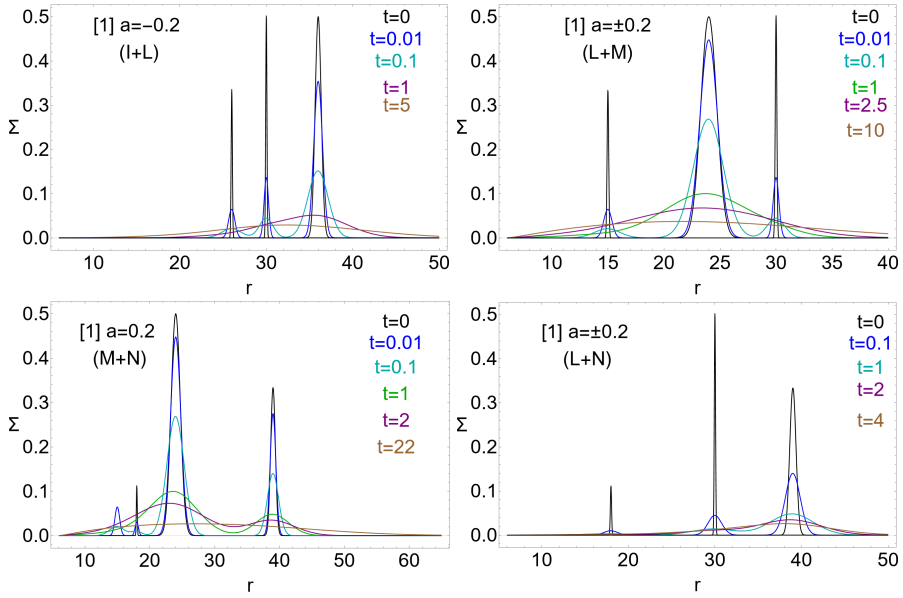

Figure 13. Combined (independent) evolution of the surface densities Σ of the ℓcounter-rotating rings couples composed by two sets of ℓco-rotating rings from the integration in Figure 12. The initial density profiles are the combinations of models $\{(\mathbf{I}), (\mathbf{L}), (\mathbf{M}), (\mathbf{N})\}$ defined in Table 2, with boundary condition $[\mathbf{1}]$ of Equation (16). ν is the viscosity coefficient. System $(\mathbf{I}+\mathbf{L})$ is the ℓco-rotating triplet of counter-rotating rings $\mathrm{C}_+(\mathbf{I}) < \mathrm{C}_+(\mathbf{L}) < \mathrm{C}_+(\mathbf{I})$. System $(\mathbf{L}+\mathbf{M})$ is the ℓcounter-rotating triplet $\mathrm{C}_-(\mathbf{M}) < \mathrm{C}_-(\mathbf{M}) < \mathrm{C}_+(\mathbf{L})$. System $(\mathbf{M}+\mathbf{N})$ is the ℓco-rotating quadruplet of co-rotating rings $\mathrm{C}_-(\mathbf{M}) < \mathrm{C}_-(\mathbf{N}) < \mathrm{C}_-(\mathbf{M}) < \mathrm{C}_-(\mathbf{N})$. System $(\mathbf{L}+\mathbf{N})$ is the ℓcounter-rotating triplet $\mathrm{C}_-(\mathbf{N}) < \mathrm{C}_+(\mathbf{L}) < \mathrm{C}_-(\mathbf{N})$. The radial range has been adapted according to the combination of the independent integrations ranges. The viscosity coefficients ν are fixed according to Figure 12.

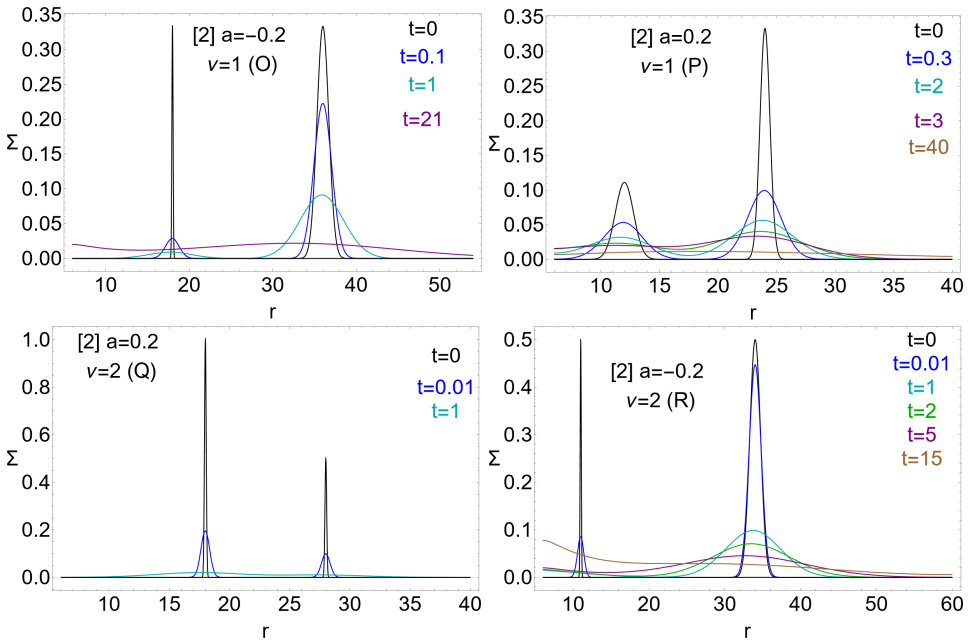

Figure 14. Evolution of the surface density Σ (ℓco-rotating rings) in the Kerr metric with spin $a = \pm 0.2$ for co-rotating and counter-rotating fluids, respectively, at different times r signed on the panels (see Table 3). The initial density profiles are the models $\{(\mathbf{O}), (\mathbf{P}), (\mathbf{Q}), (\mathbf{R})\}$ of Table 2, with the boundary condition $[\mathbf{2}]$ of Equation (16). ν is the viscosity coefficient.

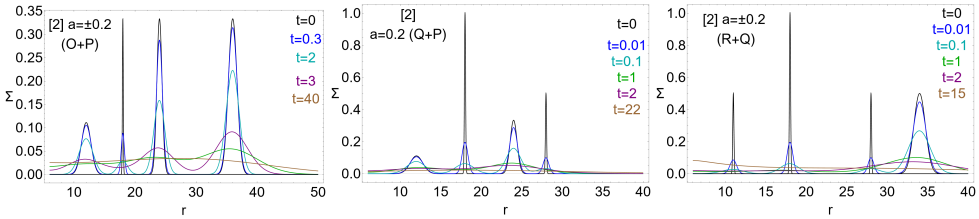

Figure 15. Combined (independent) evolution of the surface densities Σ of the ℓcounter-rotating rings couples composed by two sets of ℓco-rotating rings from the integration in Figure 14. The initial density profiles are the combinations of models $\{(\mathbf{O}), (\mathbf{P}), (\mathbf{Q}), (\mathbf{R})\}$ defined in Table 2, with boundary condition $[\mathbf{1}]$ of Equation (16). ν is the viscosity coefficient. System $(\mathbf{O} + \mathbf{P})$ is the ℓcounter-rotating quadruplet $\mathrm{C}_-(\mathbf{P}) < \mathrm{C}_+(\mathbf{Q}) < \mathrm{C}_-(\mathbf{P}) < \mathrm{C}_+(\mathbf{Q})$. System $(\mathbf{Q} + \mathbf{P})$ is the ℓco-rotating quadruplet of co-rotating rings $\mathrm{C}_-(\mathbf{P}) < \mathrm{C}_-(\mathbf{Q}) < \mathrm{C}_-(\mathbf{P}) < \mathrm{C}_-(\mathbf{Q})$. System $(\mathbf{R} + \mathbf{Q})$ is the ℓcounter-rotating quadruplet $\mathrm{C}_+(\mathbf{R}) < \mathrm{C}_-(\mathbf{Q}) < \mathrm{C}_-(\mathbf{Q}) < \mathrm{C}_+(\mathbf{R})$. The radial range has been adapted according to the combination of the independent integrations ranges. The viscosity coefficients ν are fixed according to Figure 14.

Figure 17 shows the independent evolution of ℓco-rotating rings with different viscosities. **RAD** evolution does not differ qualitatively from the ℓco-rotating solutions of the diffusive **RAD** equation.

In Figures 18 and 19, boundary conditions $[\mathbf{4}]$ of Equation (16) are applied to the models $\{(\mathbf{I}), (\mathbf{L}), (\mathbf{M}), (\mathbf{N})\}$ and can be compared to Figure 8.

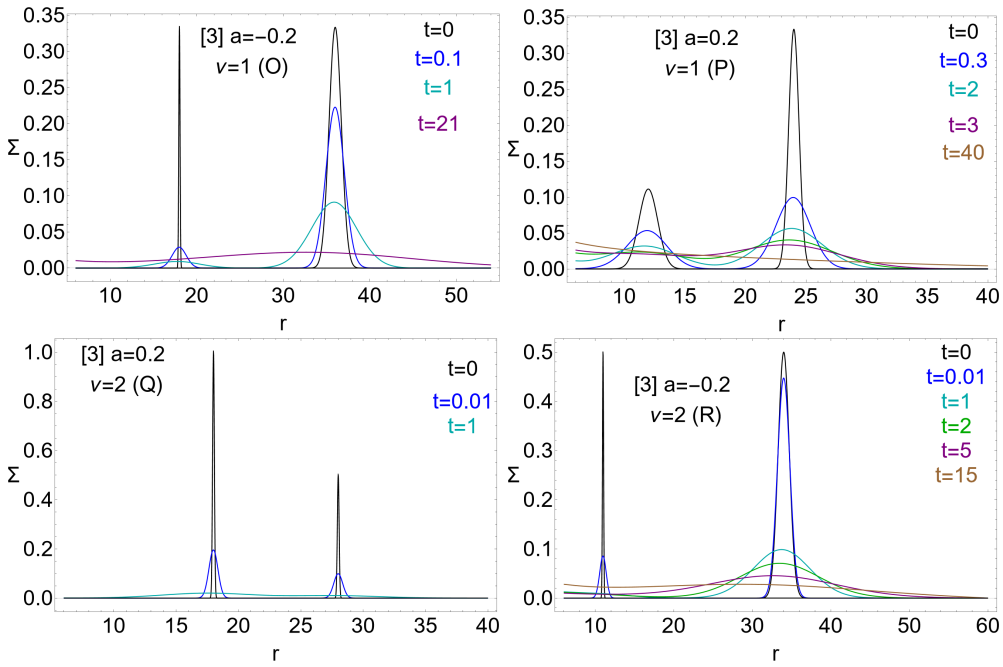

Figure 16. Evolution of the surface density Σ (ℓco-rotating rings) in the Kerr metric with spin $a = \pm 0.2$ for co-rotating and counter-rotating fluids, respectively, at different times t signed on the panels (see Table 3). The initial density profiles are the models $\{(\mathbf{O}), (\mathbf{P}), (\mathbf{Q}), (\mathbf{R})\}$ of Table 2, with the boundary condition [**3**] of Equation (16). ν is the viscosity coefficient.

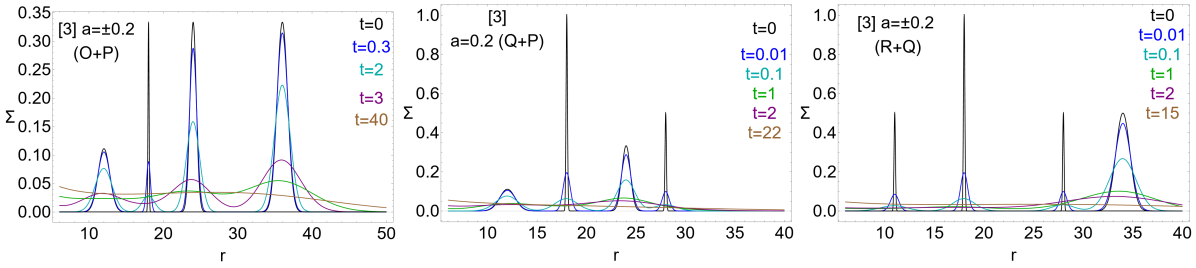

Figure 17. Combined (independent) evolution of the surface densities Σ of the ℓcounter-rotating rings couples composed by two sets of ℓco-rotating rings from the integration in Figure 16. The initial density profiles are the combinations of models $\{(\mathbf{O}), (\mathbf{P}), (\mathbf{Q}), (\mathbf{R})\}$ defined in Table 2, with boundary condition [**3**] of Equation (16). ν is the viscosity coefficient. System $(\mathbf{O} + \mathbf{P})$ is the ℓcounter-rotating quadruplet $\mathrm{C}_-(\mathbf{P}) < \mathrm{C}_+(\mathbf{Q}) < \mathrm{C}_-(\mathbf{P}) < \mathrm{C}_+(\mathbf{Q})$. System $(\mathbf{Q} + \mathbf{P})$ is the ℓco-rotating quadruplet of co-rotating rings $\mathrm{C}_-(\mathbf{P}) < \mathrm{C}_-(\mathbf{Q}) < \mathrm{C}_-(\mathbf{P}) < \mathrm{C}_-(\mathbf{Q})$. System $(\mathbf{R} + \mathbf{Q})$ is the ℓcounter-rotating quadruplet $\mathrm{C}_+(\mathbf{R}) < \mathrm{C}_-(\mathbf{Q}) < \mathrm{C}_-(\mathbf{Q}) < \mathrm{C}_+(\mathbf{R})$. The radial range has been adapted according to the combination of the independent integrations ranges. The viscosity coefficients ν are fixed according to Figure 16.

In Figure 20, $\mathcal{F}$ (the mass flux defined in Equation (11) in the Kerr spacetime with $a = \pm 0.2$ for the ℓco-rotating rings is shown at different stages of **RAD** evolution. Boundary condition [**4**] of Equation (16) has been adopted with initial models $\{(\mathbf{I}), (\mathbf{L}), (\mathbf{M})\}$ of Table 2. The related density evolution is shown in Figure 18). The flux zeros (changing slowly with time) as well as the disk spreading during **RAD** evolution and the destruction of the inner ringed density profile are evidenced.

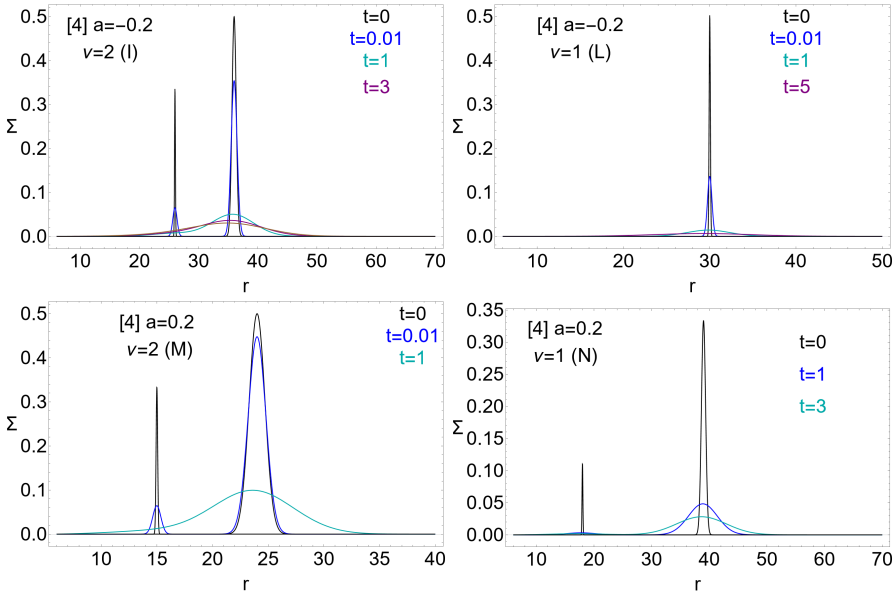

Figure 18. Evolution of the surface density Σ (ℓco-rotating rings) in the Kerr metric with spin $a = \pm 0.2$ for co-rotating and counter-rotating fluids, respectively (see Table 3). All the quantities are dimensionless. Dimensionless time values for the different stages of evolution are signed on the panel. The initial density profiles are the models $\{(\mathbf{I}), (\mathbf{L}), (\mathbf{M}), (\mathbf{N})\}$ of Table 2, with the boundary condition [**4**] of Equation (16). ν is the viscosity coefficient. Note, model $(\mathbf{L})$ (upper-right panel) is composed of one counter-rotating ring).

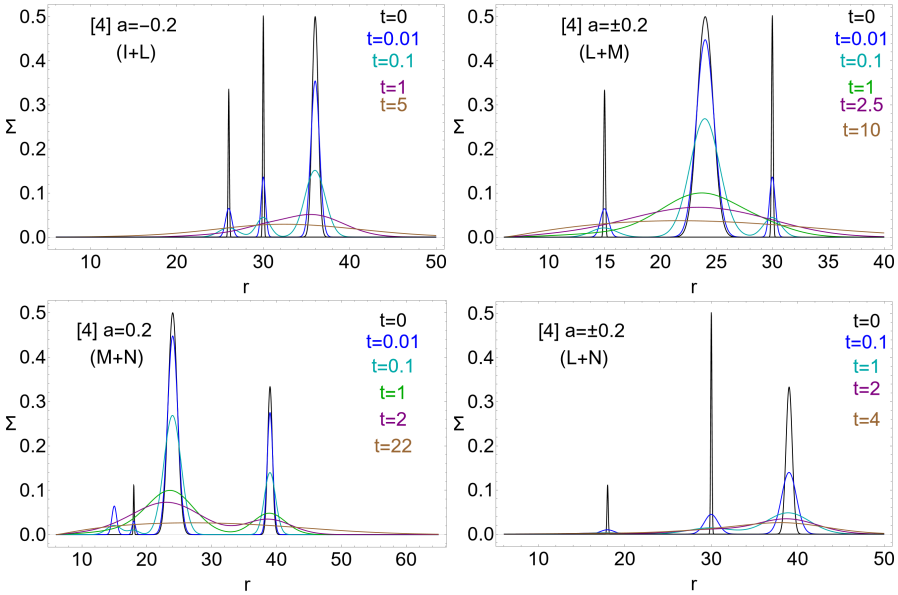

Figure 19. Combined (independent) evolution of the surface densities Σ of the ℓcounter-rotating rings couples composed by two sets of ℓco-rotating rings from the integration in Figure 18. The initial density profiles are the combinations of models $\{(\mathbf{I}), (\mathbf{L}), (\mathbf{M}), (\mathbf{N})\}$ defined in Table 2, with boundary condition [**4**] of Equation (16). ν is the viscosity coefficient. System $(\mathbf{I}+\mathbf{L})$ is the ℓco-rotating triplet of counter-rotating rings $\mathrm{C}_+(\mathbf{I}) < \mathrm{C}_+(\mathbf{L}) < \mathrm{C}_+(\mathbf{I})$. System $(\mathbf{L}+\mathbf{M})$ is the ℓcounter-rotating triplet $\mathrm{C}_-(\mathbf{M}) < \mathrm{C}_-(\mathbf{M}) < \mathrm{C}_+(\mathbf{L})$. System $(\mathbf{M}+\mathbf{N})$ is the ℓco-rotating quadruplet of co-rotating rings $\mathrm{C}_-(\mathbf{M}) < \mathrm{C}_-(\mathbf{N}) < \mathrm{C}_-(\mathbf{M}) < \mathrm{C}_-(\mathbf{N})$. System $(\mathbf{L}+\mathbf{N})$ is the ℓcounter-rotating triplet $\mathrm{C}_-(\mathbf{N}) < \mathrm{C}_+(\mathbf{L}) < \mathrm{C}_-(\mathbf{N})$. The radial range has been adapted according to the combination of independent integrations ranges. The viscosity coefficients ν are fixed according to Figure 18.

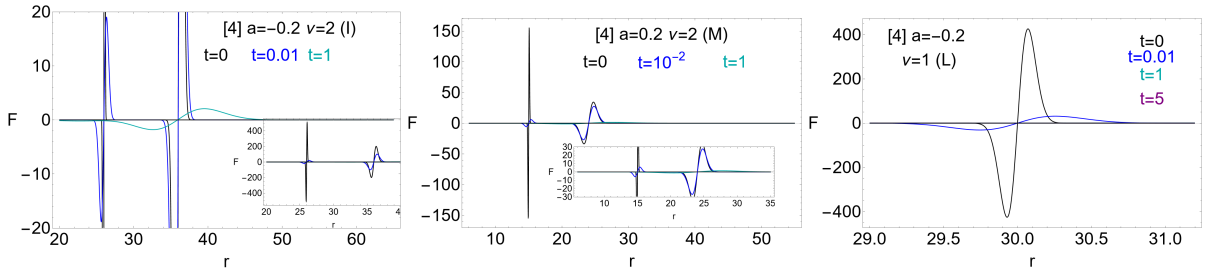

Figure 20. The mass flux $\mathcal{F}$ of Equation (11) for the ℓco-rotating rings couples in the Kerr metric with spin $a = \pm 0.2$ for co-rotating and counter-rotating fluids, respectively (see Table 3). All the quantities are dimensionless. The initial density profiles are the models $\{(\mathbf{I}), (\mathbf{L}), (\mathbf{M})\}$ of Table 2, with the boundary condition [**4**] of Equation (16). ν is the viscosity coefficient. Density evolution is shown in Figure 18.

In Figure 21, the radial drift of the fluid density Σ is considered by studying the solution $\Sigma' \equiv \partial_r \Sigma = 0$ in the plane $t - r$ for co-rotating and counter-rotating fluids orbiting the **BH** spacetime with spin $a = \pm 0.2$, respectively. The initial density profiles are models $\{(\mathbf{I}), (\mathbf{L}), (\mathbf{M})\}$ (density evolution is shown in Figure 18), with the boundary condition [**4**]. The integration ranges consider the **RAD** inner $(\mathbf{i})$, center $(\mathbf{c})$, and outer $(\mathbf{o})$ tori. The systems $(\mathcal{Q}) + (\mathcal{P})$ for the two general models $\{(\mathcal{Q}), (\mathcal{P})\}$ consider sums that are two seed evolutions apart, which is the solution of $\Sigma'(\mathcal{Q}) = 0$ and $\Sigma'(\mathcal{P}) = 0$, while system $(\mathcal{Q} + \mathcal{P})$ is the solution of $\Sigma'(\mathcal{Q}) + \Sigma'(\mathcal{P}) = 0$. The radial ranges distinguishing the $(\mathbf{i})$, $(\mathbf{c})$, and $(\mathbf{o})$ components are defined by the radii $r_{\rm IN} < r_{(c)} \leq r_* < r_\infty$. The radial drift of the inner and outer tori follows the destruction of the inner ringed structure[12]

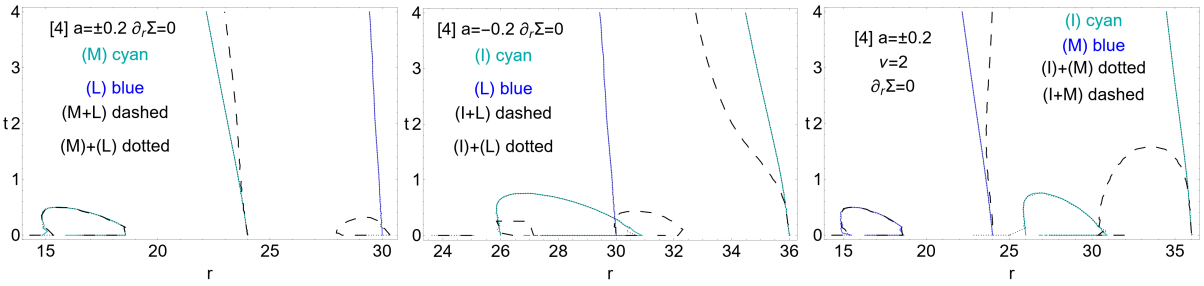

Figure 21. Radial drift of the fluid density Σ. Solution $\Sigma' \equiv \partial_r \Sigma = 0$ in the plane $t - r$ for co-rotating and counter-rotating fluids orbiting the **BH** spacetime with spin $a = \pm 0.2$, respectively (see Table 3). All quantities are dimensionless. The initial density profiles are the models $\{(\mathbf{I}), (\mathbf{L}), (\mathbf{M})\}$ of Table 2, with the boundary condition [**4**] of Equation (16). ν is the viscosity coefficient. Density evolution is shown in Figure 18. The integration ranges consider the **RAD** inner $(\mathbf{i})$, center $(\mathbf{c})$, and outer $(\mathbf{o})$ tori. The radial ranges distinguishing the $(\mathbf{i})$, $(\mathbf{c})$, and $(\mathbf{o})$ components are defined by the radii $r_{\rm IN} < r_{(c)} \leq r_* < r_\infty$. For the ℓco-rotating seeds $(\mathbf{I})$ and $(\mathbf{M})$, the inner torus $(\mathbf{i})$ is defined in the range $[r_{\rm IN}, r_*]$ and the outer torus (o) is defined in $[r_*, r_\infty]$, where the $(\mathbf{I})$ seed there is $r_* = 30$, and the $(\mathbf{M})$ seed there is $r_* = 22$. For the combined independent system $(\mathbf{M} + \mathbf{L})$, there is $(r_{(c)} = 22, r_* = 28)$, where the inner torus $(\mathbf{i})$ is defined in $[r_{\rm IN}, r_{(c)}]$; the center torus $(\mathbf{c})$ is defined in $[r_{(c)}, r_*]$; the outer torus $(\mathbf{o})$ is defined in $[r_*, r_\infty]$. The systems $(\mathcal{Q}) + (\mathcal{P})$ for two general models $\{(\mathcal{Q}), (\mathcal{P})\}$ consider the sums two evolutions apart, which is the solution of $\Sigma'(\mathcal{Q}) = 0$ and $\Sigma'(\mathcal{P}) = 0$, while $(\mathcal{Q} + \mathcal{P})$ is the solution of $\Sigma'(\mathcal{Q}) + \Sigma'(\mathcal{P}) = 0$.

In Figure 22, the evolution of the disk mass M_D of Equation (17) is studied as a function of the dimensionless time. Co-rotating and counter-rotating fluids were considered orbiting the **BH** spacetime with spin $a = \pm 0.2$, respectively (see Table 3). The initial density profiles are the models $\{(\mathbf{I}), (\mathbf{L}), (\mathbf{M})\}$ of Table 2, with the boundary condition [**4**] of Equation (16), and the related density evolution is shown in Figure 18. The systems $(\mathcal{Q}) + (\mathcal{P})$ for two general models $\{(\mathcal{Q}), (\mathcal{P})\}$ represent the sums of the two evolutions apart, which is the

sum of $M_D(\mathcal{Q})/2\pi$ and $M_D(\mathcal{P})/2\pi$, while $(\mathcal{Q}+\mathcal{P})$ is the mass of the composed system formed by $(\mathcal{Q})$ and $(\mathcal{P})$, where these two evaluations are clearly coincident. At later stages of the **RAD** disk evolution, the curves decrease approximately with a power law (t^s for s = constant). The integration ranges consider the **RAD** inner $(\mathbf{i})$, center $(\mathbf{c})$, and outer $(\mathbf{o})$ tori. There is, therefore, an exponential decrease in **RAD** mass at a later stage of **RAD** evolution, similar to one disk evolution. The decomposition with the selection of the radii $r_c < r_*$ is set here on the condition of faint density in the ring's interspace. The analysis of the **RAD** decomposition for the ℓco-rotating couples or the combined evolution of the **RAD** seeds in the inner, outer, and eventually, central ring shows the mass increase on one ring component in correspondence to the mass decreases of the other inner component following matter exchange for accretion from the outer ring to the inner one, for example, from the outer disk to the central ring or the outer ring to the inner ring, as shown in Figure 18. The outer ring mass increases at larger stages of evolution independently to the disk rotation orientation with respect to the Kerr **BH** and the relative rotation orientation.

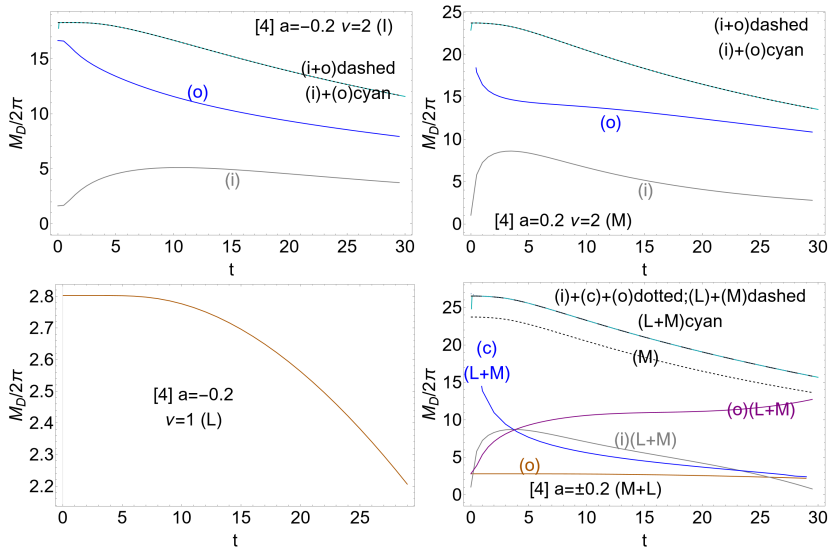

Figure 22. Evolution of the disk mass as a function of the dimensionless time. For large times, the curves decrease approximately with a power law of t^s for co-rotating and counter-rotating fluids orbiting the **BH** spacetime with spin $a = \pm 0.2$, respectively (see Table 3). All quantities are dimensionless. The initial density profiles are the models $\{(\mathbf{I}), (\mathbf{L}), (\mathbf{M})\}$ of Table 2, with the boundary condition [**4**] of Equation (16). ν is the viscosity coefficient. Density evolution is shown in Figure 18. The integration ranges consider the **RAD** inner $(\mathbf{i})$, center $(\mathbf{c})$, and outer $(\mathbf{o})$ tori. The radial ranges distinguishing the $(\mathbf{i})$, $(\mathbf{c})$, and $(\mathbf{o})$ components are defined by the radii $r_{\rm IN} < r_{(c)} \leq r_* < r_\infty$. For the ℓco-rotating seeds $(\mathbf{I})$ and $(\mathbf{M})$, the inner torus $(\mathbf{i})$ is defined in the range $[r_{\rm IN}, r_*]$, and the outer torus $(\mathbf{o})$ is defined as $[r_*, r_\infty]$, where for the $(\mathbf{I})$ seed, $r_* = 30$, and for the $(\mathbf{M})$ seed, $r_* = 22$. For the combined independent system $(\mathbf{M}+\mathbf{L})$, $(r_{(c)} = 22, r_* = 28)$, where the inner torus $(\mathbf{i})$ is defined in $[r_{\rm IN}, r_{(c)}]$; the center torus $(\mathbf{c})$ is defined in $[r_{(c)}, r_*]$; the outer torus $(\mathbf{o})$ is defined in $[r_*, r_\infty]$. The systems $(\mathcal{Q})+(\mathcal{P})$ for two general models $\{(\mathcal{Q}), (\mathcal{P})\}$ consider the sums of the two evolutions apart, which is the sum of $M_D(\mathcal{Q})/2\pi$ and $M_D(\mathcal{P})/2\pi$, while $(\mathcal{Q}+\mathcal{P})$ is the mass of the composed system formed by $(\mathcal{Q})$ and $(\mathcal{P})$ (the two evaluations clearly are coincident).

The analysis of the **RAD** seed diffusive equation in the **R**-frame is completed in Figures 23 and 24 with the initial density profiles $\{(\mathbf{I}), (\mathbf{L}), (\mathbf{M}), (\mathbf{N})\}$ of Table 2 with the boundary condition [**5**] of Equation (16). It is interesting to note that the persistence of the maximum density at later stages of evolution depends on the ring's spreading rather then the ring's density maximum.

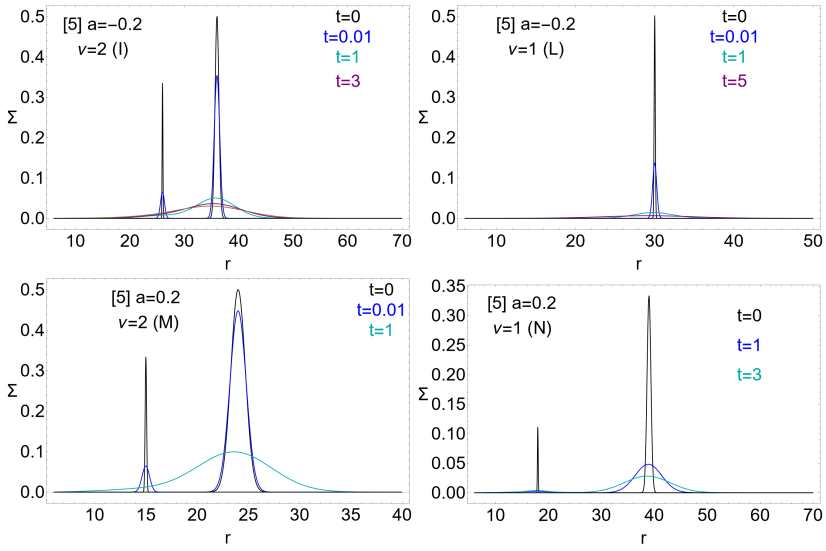

Figure 23. Evolution of the surface density Σ (ℓco-rotating rings) in the Kerr metric with spin $a = \mp 0.2$ for counter-rotating and co-rotating fluids, respectively (see Table 3). All the quantities are dimensionless. Dimensionless time values for the different stages of evolution are signed on the panel. The initial density profiles are the models $\{(\mathbf{I}), (\mathbf{L}), (\mathbf{M}), (\mathbf{N})\}$ of Table 2, with the boundary condition [**5**] of Equation (16). ν is the viscosity coefficient. Note, model $(\mathbf{L})$ (**upper-right** panel) is composed of one counter-rotating ring).

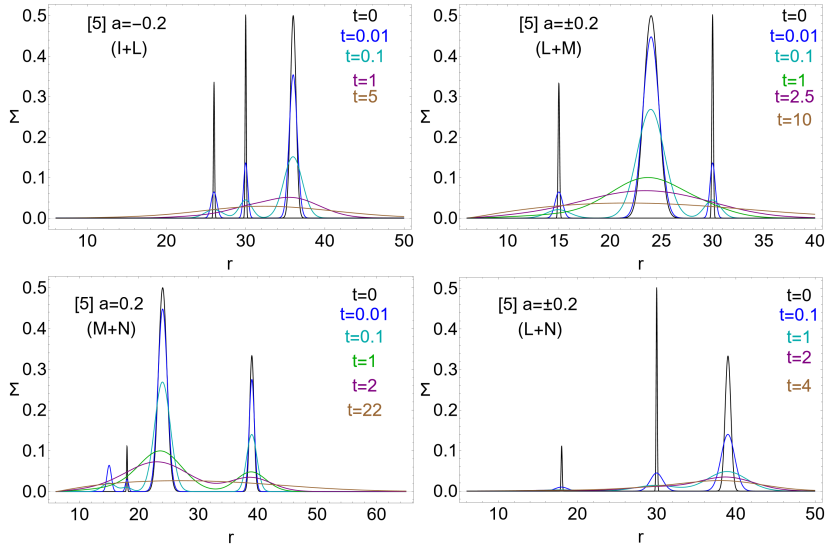

Figure 24. Combined (independent) evolution of the surface densities Σ of the ℓcounter-rotating rings couples composed by two sets of ℓco-rotating rings from the integration in Figure 23 for the Kerr spacetime with spin $a = \pm 0.2$ for co-rotating and counter-rotating fluids, respectively (see Table 3). Dimensionless time values for the different stages of evolution are signed on the panel. All the quantities are dimensionless. The initial density profiles are the combinations of models $\{(\mathbf{I}), (\mathbf{L}), (\mathbf{M}), (\mathbf{N})\}$ defined in Table 2, with boundary condition [**5**] of Equation (16). ν is the viscosity coefficient. System $(\mathbf{I} + \mathbf{L})$ is the ℓco-rotating triplet of counter-rotating rings $\mathrm{C}_+(\mathbf{I}) < \mathrm{C}_+(\mathbf{L}) < \mathrm{C}_+(\mathbf{I})$. System $(\mathbf{L} + \mathbf{M})$ is the ℓcounter-rotating triplet $\mathrm{C}_-(\mathbf{M}) < \mathrm{C}_-(\mathbf{M}) < \mathrm{C}_+(\mathbf{L})$. System $(\mathbf{M} + \mathbf{N})$ is the ℓco-rotating quadruplet of co-rotating rings $\mathrm{C}_-(\mathbf{M}) < \mathrm{C}_-(\mathbf{N}) < \mathrm{C}_-(\mathbf{M}) < \mathrm{C}_-(\mathbf{N})$. System $(\mathbf{L} + \mathbf{N})$ is the ℓcounter-rotating triplet $\mathrm{C}_-(\mathbf{N}) < \mathrm{C}_+(\mathbf{L}) < \mathrm{C}_-(\mathbf{N})$. The radial range has been adapted according to the combination of the independent integrations ranges. The viscosity coefficients ν are fixed according to Figure 23.

4. Conclusions

We discussed the evolution equation of a ringed accretion disk composed of clusters of co-rotating and counter-rotating general relativistic thin disks, solving a diffusion-like propagating equation for the **RAD** surface density. Following [1], the approach developed for a single disk is applied here to a ring agglomerate orbiting on the equatorial plane of a central Kerr **BH** and defined by an initial modulated density profile. The clusters are composed of rings of different densities and spreading. The numerical solutions of the **RAD** diffusive equations, recovered from the conservation of particle number and the toroidal component of the stress-energy tensor, have been found to test multiple viscosity prescriptions and boundary conditions. The analysis was performed considering both faster-spinning and slower-spinning **BH** spacetimes. The initial spreading of disks, constituting the internal ringed structure, governs the **RAD** evolution, being a predominant factor with respect to the initial ring densities.

It was found that the first stage of the cluster evolution involves inner structure dynamics and is characterized by spreading in the **RAD** and the modification of the internal structure disappearing in the second stage, while the third stage is dominated by the formation of a single disk with an internal density maximum. The final stage of **RAD** evolution is characterized by single-disk evolution at the origin. We focused mostly on the first stages of evolution. Close to the last stable circular radius, for small density Σ, our analysis shows that the disks evolve similarly to the non-relativistic case (see also [17]).

The investigation first focused on the evolution of a set of ℓcounter-rotating or ℓco-rotating sets subjected to several viscosity prescriptions and boundary conditions, defined by an initial modulated density profile governing the inner ringed structure of the **RAD**. We then analyzed the combined independent evolution of the ℓcounter-rotating seeds. In this combined analysis, the radial range of integration was fixed considering the two seeds' different inner edges. The combination of the ℓcounter-rotating seeds shows that the evolution is qualitatively similar to the ℓco-rotating evolution. However, we proved the persistence of an inner ringed structure also at later times, while the internal dynamics (characterized by ring component interaction) do not affect the **RAD** boundary region's evolution.

Hence, the analysis explores wide ranges of different cases, selected in the classes (of possible configurations) relevant to the phenomenological impact, especially for the astrophysical context of **SMBHs** and their accretion disk evolution. Therefore, we analyzed, among the different cases, the following: *(1)* differences for fast and slowly spinning **BHs**, *(2)* the impact of tori number, *(3)* the divergences between ℓco-rotating and ℓcounter-rotating tori, and *(4)* the effects of different viscosities and boundary conditions. The astrophysical differences evidenced in the disk density evolution for each different case are dominated by the different relative rotations of the tori and the density differences in the initial ringed density. These aspects affect the timescales of the process and characterize the final phases of **RAD** evolution, which are constituted by one single disk resulting from the multi-tori merger. We go into detail below, summarizing the impact of each different condition on the final evolution. Note that the aggregates of different disks with different viscosity are equivalent, in our frame, to a single disk affected by inhomogeneous viscosity (depending on the radius) and with possibly different rotation orientation in the (single) ringed profile. However, for the astrophysical context, the most impacting feature appears during composed (independent) evolution, which can be split into the contribution of different components (as in Figure 22), evident in the mass accretion rate. The effects of disk morphology as the set of several systems are then evident in all the phenomena associated with the existence of the multiple *inter-disk inner-edges*. The relative rotation and initial difference in density, differentiated particularly in the spacetimes of the faster spinning attractors, are, also in this frame, the most relevant factors influencing the process timescales.

The evolution of the disk mass M_D, mass flux, and radial drift was also studied as a function of the dimensionless time, in dependence on the ring rotation orientation, **BH** spin, and the initial **RAD** density profile. The mass increases on one ring component, and

in correspondence, the mass decreases the other inner component, mostly independent from the ring's relative rotation orientation and rotation with respect to the central **BH**. At later stages, the curves M_D decrease approximately with a power law (t^s for s =constant) (within the condition of faint density in the rings interspace). On the other hand, focusing on the initial stages of the seed evolution featuring the **RAD** inner structure evolution with rings interaction, the process timescales of the inner ringed structure re-modulation depend on the initial rings spreading and density (the process appears less dependent on the different viscosity values, in the first approximation the viscosity appears most relevant factor when the viscosity fluctuation in the **RAD** distribution is the greater). The disk in this stage can retain a modulated inner density profile depending on the tori's initial spreading and separation (see, for example, model (**D**)).

However, it should be noted that, while in this analysis stress models have been applied in the entire range of integration, other conditions should apply at infinity, particularly in the inner region (for $r \in]r_+, r_{\rm IN}[$). In fact, in the **RAD**, the perturbation analysis is complicated by the typical inter-disk activity constituted by the inter-ring accretion and disk collision. More generally, the presence of multiple inner edges, due to the internal ringed structure, undermines the validity of the use of viscosity as a perturbation for the only non-zero radial fluid velocity. That is, it exists as an unperturbed component $\tilde{U}^r \neq 0$ in the presence of radial inter-disk flux.

Furthermore, for fast-spinning attractors ($a > 0.828427$), the co-rotating ring is expected to partially orbit the outer ergoregion of the Kerr spacetime, and for faster-spinning attractors ($a > 0.942809$), the inner edge of the inner co-rotating ring is expected to be in the outer-ergoregion, and the ring can be totally contained in this region. In this situation, the counter-rotating flow from the outer disk, having an initial toroidal velocity $u^\phi < 0$, arrives at the outer ergosurface with $u^\phi > 0$. The flow is free-falling and there is a constant $\ell < 0$ along all the motion. Therefore, the flow crosses, and before reaching the outer ergosurface, an inversion surface embeds the central **BH**, where $u^\phi = 0$, which is defined by the parameter ℓ. Consequently, in the presence of an inner co-rotating disk, the counter-rotating flow from the outer torus can impact the inner ring with $u^\phi > 0$ [21].

However, within all these approximations, our analysis is a feasible test of the early stages of **RAD** evolution. For all these reasons, this early exploratory study provided a preliminary but well-founded overview of the multi-ring frame of ring aggregate evolution.

We stress the possibility of accretion rings being produced by tidal disruptions of multiple stellar systems when they sink too close to the **SMBH**. In this frame, our application could be extremely timely in connection with the recent apparent detection of the the first binary star in the S-cluster close to SgrA* [22].

Author Contributions: Conceptualization, D.P., Z.S. and V.K. All authors have contributed to the article and have agreed to the published version of the manuscript.

Funding: This research received no external funding.

Data Availability Statement: No new data were used or generated in this article.

Conflicts of Interest: The authors declare no conflicts of interest.

Appendix A. On the Null Flux Condition

Here, we include some notes on the condition of the null flux $\mathcal{F}$, which was explored in Section 3.

Condition $\mathcal{F} = 0$ at point r implies ($\Sigma = 0$, $\Sigma' = 0$) or $\Sigma' = 0$ for r on a particular orbit $r^{\pm}_{\odot}$ for counter-rotating and co-rotating fluids, respectively. Radius $r^{-}_{\odot}$ is the zero of $R^{-}_{\odot} \equiv 8a^3 + a^2(7r - 15)\sqrt{r} - 8ar^2 + [6 - (r - 3)r]r^{3/2}$ for the co-rotating case, and $r^{+}_{\odot}(a)$ is the zero of the quantity $R^{+}_{\odot}(a) \equiv R^{-}_{\odot}(-a)$ for the counter-rotating case. Radii $r^{\pm}_{\odot}(a)$ are shown in Figure A1. Interestingly, this radius strongly distinguishes the co-rotating from the counter-rotating fluxes. This property is particularly relevant for the **RAD**, where the flux from the outer and inner torus is considered in the region $r < r^{\pm}_{mso}$. As is clear

from Figure A1, there is $r^{+}_{\odot} \in]r^{+}_{mbo}, r^{+}_{mso}[$ for any $a \in [0,1]$, which is not always the case for co-rotating fluxes where condition $r^{-}_{\odot} \in]r^{-}_{mbo}, r^{-}_{mso}[$ holds for $a \in [0, a_{\odot}]$, where at $a_{\odot} \equiv 5/9$, there is $r^{-}_{\odot} = r^{-}_{mbo}$. For larger spin, $a > a_{\odot}$, where $r^{-}_{\odot} \in [r^{-}_{\gamma}, r^{-}_{mbo}]$. Furthermore, for **BH** spin, $a_{\propto} = 0.8117$ and there is $r^{-}_{\odot} = r^{+}_{\epsilon}$; therefore, the (co-rotating) flux has a zero point in the ergoregion for **BH** spin $a > a_{\propto}$. This aspect can also play a relevant role for ℓ counter-rotating systems for slower spin **BHs** for the case when the disk is counter-rotating.

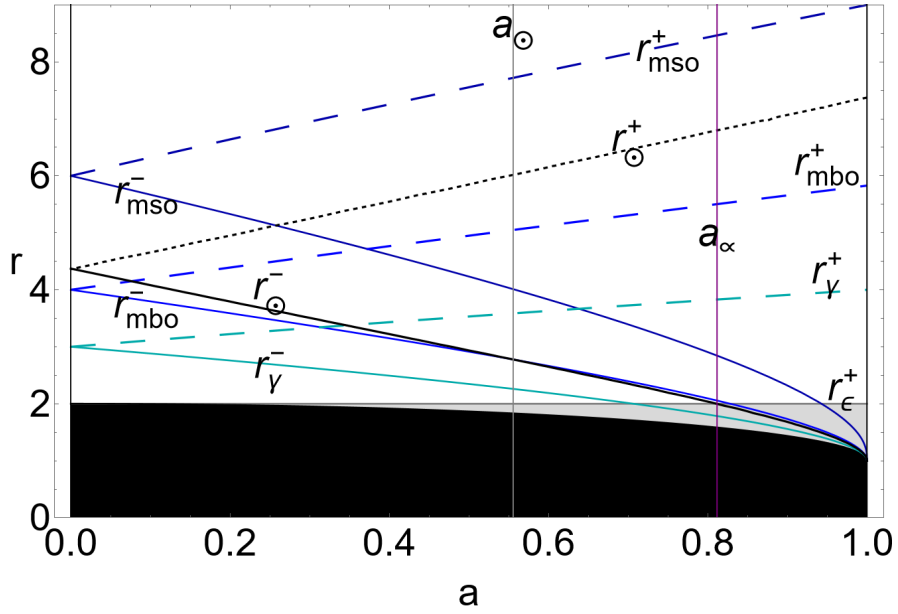

Figure A1. On the null flux $\mathcal{F}$ condition: Appendix A. Radii $r^{\pm}_{\odot}$ for counter-rotating and co-rotating fluids, respectively, are plotted as functions of the central Kerr **BH** spin $a \in [0,1]$. All quantities are dimensionless. On $r^{\pm}_{\odot}$, there is $\mathcal{F} = 0$ with $\Sigma' = 0$. The black region is $r < r_{+}$, with r_{+} being the outer horizon of the Kerr geometry, and the gray region is $r < r^{+}_{\epsilon}$, where $r^{+}_{\epsilon} = 2M$ is the outer ergosurface on the attractor equatorial plane. The geodesic structure of the Kerr spacetime is also plotted: radius $r^{\pm}_{mso}$ is the marginally stable orbit, $r^{\pm}_{\gamma}$ is the marginally circular orbit, and $r^{\pm}_{mbo}$ is the marginally bounded orbit for counter-rotating and co-rotating particles, respectively. At $a_{\propto} = 0.8117$, there is $r^{-}_{\odot} = r^{+}_{\epsilon}$.

Notes

1 We adopt the geometrical units $c = 1 = G$ and the $(-,+,+,+)$ signature, Latin indices run in $\{0,1,2,3\}$. The radius r has a unit of mass $[M]$, angular momentum units of $[M]^2$, velocities $[U^t] = [U^r] = 1$, and $[U^{\phi}] = [U^{\theta}] = [M]^{-1}$ with $[U^{\phi}/U^t] = [M]^{-1}$ and $[U_{\phi}/U_t] = [M]$. For the sake of convenience, considering the dimensionless energy, effective potential $[V_{eff}] = 1$, and an angular momentum per unit of mass $[L]/[M] = [M]$.

2 It is assumed that the time scale of the dynamical processes τ_{dyn} (regulated by the gravitational and inertial forces, the timescale for pressure to balance the gravitational and centrifugal force) is much lower than the timescale of the thermal ones τ_{the} (i.e., heating and cooling processes, the timescale of radiation entropy redistribution) that is lower than the time scale of the viscous processes τ_{vis}, and the effects of strong gravitational fields are dominant with respect to the dissipative ones and predominant to determine the unstable phases of the systems [18,19], i.e., $\tau_{dyn} \ll \tau_{the} \ll \tau_{vis}$ see also [20]. Thus, the effects of strong gravitational fields dominate the dissipative ones [18,19]. Consequently, during the evolution of dynamical processes, the entropy distribution depends on the initial conditions of the system. The entropy is constant along the flow. According to the von Zeipel condition, the surfaces of constant angular velocity Ω and of constant specific angular momentum ℓ coincide, and the rotation law $\ell = \ell(\Omega)$ is independent of the equation of state. More precisely, these structures are radiation pressure-supported accretion tori, cooled by advection, with low viscosity, opaqueness, and super-Eddington luminosity (high matter accretion rates) [19]. The accretion mechanism in these models occurs from a Roche lobe overflow from the tori cusps, constituting also an important local stabilizing mechanism against thermal and viscous instabilities and globally against the Papaloizou–Pringle instability.

3 The rest of energy densityρ could include a thermal contribution, which is, in general, ignored in the thin disk approximation. The quantity p could be considered the total pressure (radiation and HD pressure).

[4] Ignoring terms higher than z^2/r^2, we adopt a near-equatorial plane approximation using the height-integrated quantities, allowing a $1+1$-dimensional analysis of the diffusive equations within the condition

$$\Sigma|_{t=0} \equiv \Sigma_0(r) \quad \text{and} \quad U^{\mathbf{x}}|_{t=0} \equiv U_0^{\mathbf{x}}(r),\ \mathbf{x} = \{t, r, \phi\}, \quad (\text{where} \quad U^a \equiv \tilde{U}^a + \xi^a, \quad \tilde{U}^a \xi_a = 0),$$

where ξ^a represents the fluctuation contribution to the mean flow, and notation $\tilde{U}^a$ is adopted for the unperturbed geodesic fluid circular velocity

[5] Assuming $a = 0$ (the static Schwarzschild case) and considering the first order in $M = 0$, we obtain the non-relativistic evolution equation:

$$\partial_t \Sigma = 3\nu \left[\frac{3\partial_r \Sigma}{2r} + \partial_r^2 \Sigma \right] = \frac{3}{r} \frac{\partial}{\partial r} \left[\sqrt{r} \partial_r \left(\nu \sqrt{r} \Sigma \right) \right];$$

see [4,5]

[6] Note, for the single disk, with time $\bar{t} = \nu t / M^2$, we can assume a constant viscosity ν, which is equivalent to the condition $M = 1$. However, for the multi-ring case it is convenient to specify the viscosity prescription for each ring explicitly.

[7] Note, the **RAD** inner edge $r_{\rm IN} \leq r_{mso}$ coincides, for a ℓco-rotating seed, with the inner edge of the most internal disk.

[8] In [1], it is assumed $r_{\rm IN}^- = r_{mso}^-$(co-rotating fluids) with $\Sigma(r_{\rm IN}) = 0$ and $\mathcal{F}(r_\infty) = 0$. Conditions on the flux at r_{mso} imply a discussion on the density Σ and its radial derivative Σ' in r_{mso}. The condition of null flux $\mathcal{F}$ and null density Σ at a point r, for example, $r_{\rm IN}$ or in the limit r_∞, are not equivalent. Conditions in r_{mso} depend on the central **BH** spin. A null flux at r_{mso} implies more restrictive conditions on the density Σ and its radial derivative Σ' at r_{mso}. At infinity, a null flux leads to $\Sigma = 0$ and $r\partial_r \Sigma = 0$. Using boundary condition $\Sigma = 0$ at the inner edge would imply neglecting the viscous torque in the region $]r_+, r_{\rm IN}[$, assuming accretion onto the central **BH** occurs in the free-falling hypothesis. Condition $\mathcal{F} = 0$ at a point r implies $\Sigma = 0$ and $\Sigma' = 0$ or, interestingly, $\Sigma' = 0$ for r on a particular orbit (see Appendix A).

[9] Time t_f is the total simulation time, and the choice of r_∞ is clearly related to numerical integration, location, spreading of the outer disk, and the choice of t_f.

[10] Here, U^t is the unperturbed velocity component, and M_D could be considered from the time integral of the flux function $\mathcal{F}$ at a proper radius.

[11] It should be stressed that this divergence with respect to the perturbation set-up adopted here is expected to be more relevant for ℓcounter-rotating rings.

[12] For ℓcounter-rotating seed analysis, the radial range split could also be implemented by considering the radius r, where the mass flux $\mathcal{F}$ changes sign (see Figures 20 and 21).

References

1. Riffert, H. The Dynamics of a Viscous Gas Ring around a Kerr Black Hole. *Astrophys. J.* **2000**, *529*, 119–126. [CrossRef]
2. Pugliese, D.; Stuchlík, Z. Ringed accretion disks. *Astrophys. J. Suppl. Ser.* **2015**, *221*, 25. [CrossRef]
3. Peissker, F.; Zajaček, M.; Labadie, L.; Bordier, E.; Eckart, A.; Melamed, M.; Karas, V. A Binary System in the S Cluster Close to the Supermassive Black Hole Sagittarius A*. *Nat. Commun.* 2024, *accepted*. Available online: https://www.nature.com/ncomms/ (accessed on 17 October 2024).
4. Lynden-Bell, D.; Pringle, J.E. The evolution of viscous discs and the origin of the nebular variables. *Mon. Not. R. Astron. Soc.* **1974**, *168*, 603–637. [CrossRef]
5. Pringle, J.E. Accretion discs in astrophysics. *Annu. Rev. Astron. Astrophys.* **1981**, *19*, 137–162. [CrossRef]
6. Nixon, C.J.; Pringle, J.E. Accretion disks with non-zero central torque. *New Astron.* **2021**, *85*, 101493. [CrossRef]
7. Frank, J.; King, A.; Raine, D.J. *Accretion Power in Astrophysics*, 3rd ed.; Cambridge University Press: Cambridge, UK, 2002.
8. Balbus, S.A. The general relativistic thin disk evolution equation. *Mon. Not. R. Astron. Soc.* **2017**, *471*, 4832–4838 [CrossRef]
9. Balbus, S.A.; Mummery, A. The evolution of Kerr disks and late-time tidal disruption event light curves. *Mon. Not. R. Astron. Soc.* **2018**, *481*, 3348–3356. [CrossRef]
10. Balbus, S.A.; Mummery, A. An upper observable black hole mass scale for tidal destruction events with thermal X-ray spectra. *Mon. Not. R. Astron. Soc.* **2021**, *505*, 1629–1644.
11. Mummery, A.; Balbus, S.A. The spectral evolution of disk dominated tidal disruption events. *Mon. Not. R. Astron. Soc.* **2000**, *492*, 5655–5674. [CrossRef]
12. Mummery, A. A unified model of tidal destruction events in the disk-dominated phase. *arXiv* **2021**, arXiv:2104.06212.
13. Mummery, A.; Balbus, S.A. Evolution of relativistic thin disks with a finite ISCO stress—I. Stalled accretion. *Mon. Not. R. Astron. Soc.* **2019**, *489*, 132–142. [CrossRef]
14. Perego, A.; Dotti, M.; Colpi, M.; Volonteri, M. Mass and spin co-evolution during the alignment of a black hole in a warped accretion disc. *Mon. Not. R. Astron. Soc.* **2009**, *399*, 2249–2263. [CrossRef]
15. Mayer, M.; Pringle, J.E. Variability of black hole accretion disks: The cool, thermal disk component. *Mon. Not. R. Astron. Soc.* **2006**, *368*, 379–396. [CrossRef]

16. Falcke, H.; Melia, F. Accretion disk evolution with wind infall. 1. General solution and application to Sgr A*. *Astrophys. J.* **1997**, *479*, 740. [CrossRef]
17. Pugliese, D.; Stuchlik, Z.; Karas, V. Notes on the general relativistic viscous ringed disc evolution. *Mon. Not. R. Astron. Soc.* **2024**, *534*, 2875–2893.
18. Font, J.A.; Daigne, F. On the stability of thick accretion disks around black holes. *Astrophys. J.* **2002**, *581*, L23–L26. [CrossRef]
19. Abramowicz, M.A.; Fragile, P.C. Black Hole Accretion Disks. *Living Rev. Relativ.* **2013**, *16*, 1. [CrossRef] [PubMed]
20. Fragile, P.C.; Blaes, O.M.; Anninos, P.; Salmonson, J.D. Global General Relativistic MHD Simulation of a Tilted Black-Hole Accretion. *Astrophys. J.* **2007**, *668*, 417–429. [CrossRef]
21. Pugliese, D.; Stuchlik, Z. Inter–disks inversion surfaces. *Eur. Phys. J. C* **2024**, *84*, 1082. [CrossRef]
22. Peißker, F.; Eckart, A.; Zajaček, M.; Ali, B.; Parsa, M. Indications of a Population of Faint Fast-moving Stars inside the S2 Orbit–S4711 on a 7.6 yr Orbit around Sgr A*. *Astrophys. J.* **2020**, *899*, 50. [CrossRef]